

10

Gravity Flow on Steep Slope

CHRISTOPHE ANCEY

10.1 Introduction

Particle-laden, gravity-driven flows occur in a large variety of natural and industrial situations. Typical examples include turbidity currents, volcanic eruptions, and sandstorms (see Simpson 1997 for a review). On mountain slopes, debris flows and snow avalanches provide particular instances of vigorous dense flows, which have special features that make them different from usual gravity currents. Those special features include the following:

- They belong to the class of non-Boussinesq flows since the density difference between the ambient fluid and the flow is usually very large, whereas most gravity currents are generated by a density difference of a few percent.
- Whereas many gravity currents are driven by pressure gradient and buoyancy forces, the dynamics of flows on slope are controlled by the balance between the gravitational acceleration and dissipation forces. Understanding the rheological behavior of particle suspensions is often of paramount importance when studying gravity flows on steep slope.

This chapter reviews some of the essential features of snow avalanches and debris flows. Since these flows are a major threat to human activities in mountain areas, they have been studied since the late 19th century. In spite of the huge amount of work done in collecting field data and developing flow-dynamics models, there remain great challenges in understanding the dynamics of flows on steep slope and, ultimately, in predicting their occurrence and behavior. Indeed, these flows involve a number of complications such as abrupt surge fronts, varying free and basal¹ surfaces, and flow structure that changes with position and time.

Subaqueous landslides and debris avalanches have many similarities with subaerial debris flows and avalanches (Hampton et al. 1996). The correspondence, however, is not complete since subaqueous debris flows are prone to hydroplane and transform into density currents as a result of water entrainment (Elverhøi et al. 2005); the slope range over which they occur is also much wider than the slope range for subaerial

¹ The basal surface is the interface between the bottom of the flow and the ground/snowcover.

flows. Powder-snow avalanches are related to turbidity currents on the ocean floor (Parker et al. 1986) and pyroclastic flows from volcanoes (Huppert and Dade 1998; Bursik et al. 2005). Powder-snow avalanches sometimes experience a rapid deceleration of their dense cores, which eventually separate from their dilute clouds and form stepped thickness patterns in their deposits. This behavior is also seen with submarine flows and pyroclastic flows. In addition to being non-Boussinesq flows, powder-snow avalanches differ from submarine avalanches in that they are closer to fixed-volume, unsteady currents than to the steady density currents with constant supply.

10.2 A Physical Picture of Gravity Flows

10.2.1 Debris Flows

Debris flows are mass movements of concentrated slurries of water, fine solids, rocks, and boulders (Iverson 1997; 2005). They are highly concentrated mixtures of sediments and water, flowing as a single-phase system on the bulk scale. Debris flows look like mudslides and landslides, but the velocities and the distances they travel are much larger. They differ from floods in sediment transport in that they are characterized by a very high solids fraction (mostly exceeding 80%).

There are many classifications of debris flows and related phenomena based on compositions, origins, and appearances. Many events categorized as “mudflows,” “debris slides,” lahars, and “hyperconcentrated flows” can be considered as particular forms of debris flows (Fannin and Rollerson, 1993; Iverson, 1997). Debris flows may result from the following:

- Mobilization from a landsliding mass of saturated unsorted materials, often after heavy and/or sustained rainfalls (Iverson et al. 1997)
- Transformation from a sediment-laden water flood into a hyperconcentrated flow, probably as a result of channel-bed failure (Tognacca 1997)
- Melting of ice and snow induced by pyroclastic or lava flows and accompanied by entrainment of large ash volumes (Voight 1990)
- Collapse of a moraine-dammed lake generating an outburst flood (Clague and Evans 2000).

The material volume mobilized by debris flows ranges from a few thousands cubic meters to a few millions, exceptionally a few billions. The velocity is typically a few meters per second, with peak velocities as high as 10 m/s (VanDine 1985; Major and Pierson 1992; Hürlimann et al. 2003). Debris flows usually need steep slopes (i.e., in excess of 20%) to be initiated and to flow, but occasionally they have been reported to travel long distances over shallow slopes (less than 10%).

Figure 10.1 shows two deposits of debris flows. In Figure 10.1a, a debris flow involving well-sorted materials embedded in a clayey matrix came to a halt on an

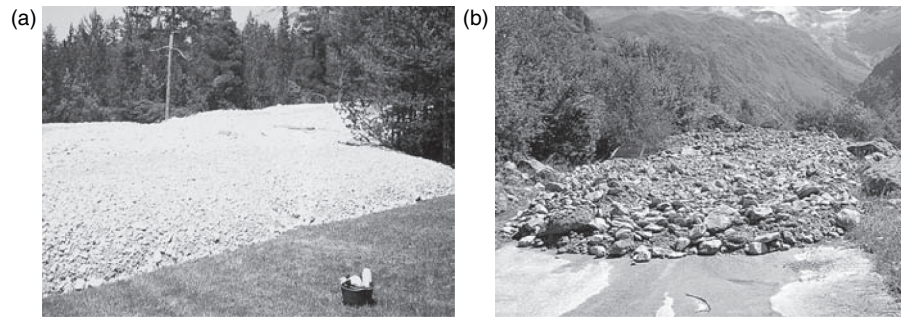


Figure 10.1. (a) Debris-flow deposit in the Ravin-des-Sables watershed (France); the bucket gives a scale of the deposit thickness. (b) Debris flow on the road to la-Chapelle-en-Valgaudemar (France). For a color version of this figure please see the color plate section.

alluvial fan²; note that there was no water seepage, which implies that the material was still water-saturated a few hours after stoppage. Figure 10.1b shows a car hit by a debris flow made up of coarse material; the conspicuous streaks of muddy water indicate that water and the finest grain fraction separated from the coarsest grain fraction as soon as the flow approached the arrested state.

10.2.2 Snow Avalanches

Avalanches are rapid, gravity-driven masses of snow moving down mountain slopes. Many, if not most, catastrophic avalanches follow the same basic principle: Fresh snow accumulates on the slope of a mountain until the gravitational force at the top of the slope exceeds the binding force holding the snow together. A solid slab of the surface layer of snow can then push its way across the underlying layer, resulting in an avalanche. The failure may also arise from a temperature increase, which reduces snow cohesion. Typically, most avalanches travel for a few hundred meters at a rather low velocity (a few meters per second), but some can move up to 15 km and achieve velocities as high as 100 m/s. They can also pack an incredible punch, up to several atmospheres of pressure. It is helpful to consider two limiting cases of avalanches depending on the flow features (de Quervain 1981):

- The *flowing avalanche*: A flowing avalanche is an avalanche with a high-density core at the bottom. Trajectory is dictated by the relief. The flow depth does not generally exceed a few meters (see Figure 10.2a). The typical mean velocity ranges from 5 to 25 m/s. On average, the density is fairly high, generally ranging from 150 to 500 kg/m³.
- The *powder snow avalanche*: It is a very rapid flow of a snow cloud, in which most of the snow particles are suspended in the ambient air by turbulence (see Figure 10.2b). Relief has usually weak influence on this aerial flow. Typically, for the flow depth, mean velocity, and mean density, the order of magnitude is 10–100 m, 50–100 m/s, 5–50 kg/m³, respectively.

² An alluvial fan is a fan-shaped deposit formed typically at the exit of a canyon, as a result of the sudden change in the bed gradient, which causes massive sediment deposition.

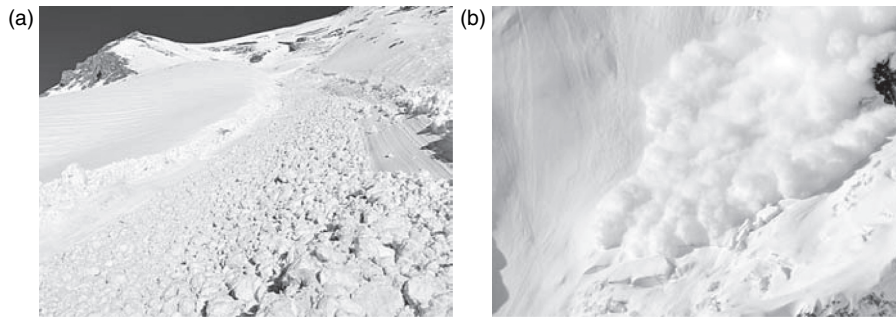


Figure 10.2. (a) Wet-snow avalanche deposit in the southern face of Grammont (Switzerland); the snowballs are approximately 10 cm in diameter. (b) Powder-snow avalanche in the northern face of Dolent (Switzerland); the typical flow depth is 20 m. For a color version of this figure please see the color plate section.

10.3 Anatomy of Gravity Currents on Slope

Knowing how a gravity-driven flow is organized is of paramount importance to understanding its properties. Contrary to most fluid-mechanics problems in which the fluid volume is bounded or infinite, a gravity current is characterized by moving boundaries:

- The free surface at the interface with the ambient air and
- The surface of contact with the ground (or snow cover), where much of the energy dissipation occurs.

These boundaries can be passive (i.e., they mark the boundaries of the volume occupied by the flowing material). On some occasions, they may be active (e.g., by promoting mass and momentum exchanges with the ambient fluid and/or the bed). Also, a gravity-driven flow often is split into three parts: the head at the leading edge, the body, and the tail. The structure of these regions depends on the material and flow properties. It is quite convenient to consider two end members of gravity flows to better understand their anatomy: debris flows are typical of dense granular flows, for which the ambient fluid has no significant dynamic role, whereas powder-snow avalanches are typical of flows whose dynamics are controlled to a large extent by the mass and momentum exchanges at the interfaces.

10.3.1 Anatomy of Debris Flows

On the whole, debris flows are typically characterized by three regions, which can change with time (see Figure 10.3):

- At the leading edge, a granular front or snout contains the largest concentration of big rocks; boulders seem to be pushed and rolled by the body of the debris flow. The front is usually higher than the rest of the flow. In some cases, no front is observed because the body has

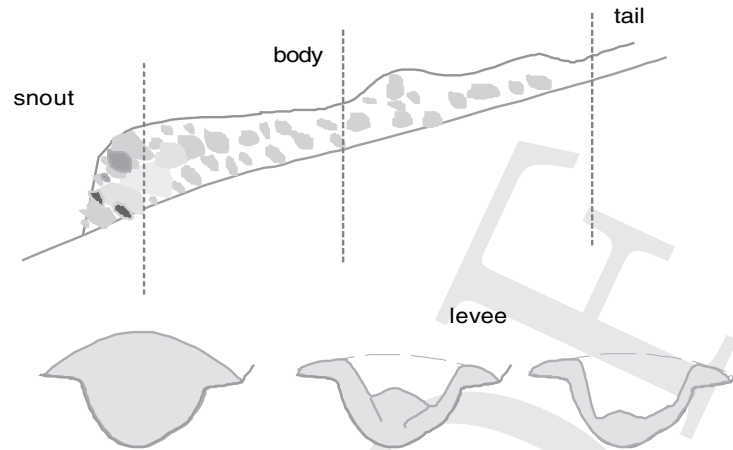


Figure 10.3. Idealized representations of a debris flow (longitudinal profile and cross-section). The different sections correspond to the dashed lines of the upper panel. Adapted from Johnson and Rodine (1984).

overtaken (a frequent occurrence when the debris flow spreads onto the alluvial fan) or because the materials are well sorted and no significant variation in the bulk composition can be detected.

- Behind the front, the body is the flow of a rock and mud mixture. Usually, the debris flow body is not in a steady state but presents unsteady surges (Zanutigh and Lamberti 2007). It can transport blocks of any size. Many authors have reported that boulders of relatively small size seem to float at the free surface, while blocks of a few meters in size move merely by being overturned by the debris flow. The morphological characteristics of the debris flow are diverse depending on debris characteristics (size distribution, concentration, mineralogy) and channel geometry (slope, shape, sinuosity, width). Flowing debris can resemble wet concrete, dirty water, or granular material, but irrespective of the debris characteristics and appearance, viscosity is much higher than for water. Most of the time, debris flows move in a completely laminar fashion, but they can also display minor turbulence; on some occasions, part of the debris flow may be highly turbulent.
- In the tail, the solid concentration decreases significantly and the flow looks like a turbulent muddy water flow.

In recent years, many outdoor and laboratory experiments have shed light on the connections existing between particle-size distribution, water content, and flow features for fixed volumes of bulk material (Davies 1986; Iverson 1997; Parsons et al. 2001; Chambon et al. 2009). In particular, experiments performed by Parsons et al. (2001) and Iverson (1997) have shown that the flow of poorly sorted materials was characterized by the coexistence of two zones, each with a distinctive rheological behavior: the flow border was rich in coarse-grained materials, whereas the core was fine grained. This self-organization has a great influence on the flow behavior; notably, the flow core behaves more like a viscoplastic material, while the flow region close

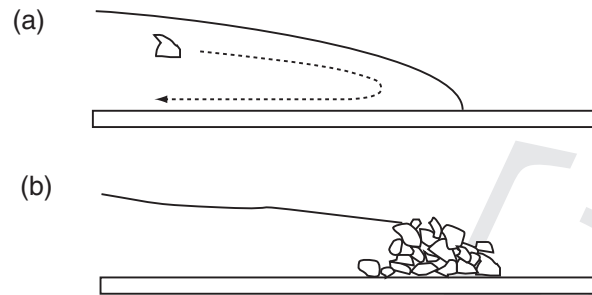


Figure 10.4. Schematic of the behavior contrast between fine-grained and coarse-grained flows. (a) Conveyer-belt-like flow at the front. (b) Formation of a frictional front. After Parsons et al. (2001).

to the levees (lateral deposits) are in a Coulomb frictional regime (sustained solid frictional contacts between grains). Moreover, the runout distance can be significantly enhanced as a result of levee formation limiting lateral spreading and energy dissipation.

Parsons et al. (2001) ran a series of experiments to investigate the effect of the composition (i.e., the importance of the finest- and coarsest-grain fractions). They used a semicircular inclined flume and measured the velocity profile at the free surface. Different slurries were prepared by altering the sand, clay, and silt fractions. They obtained muddy slurries when the matrix was rich in silt and clay, and poorly sorted mixtures when the silt and clay contents were reduced. Surprisingly enough, the change in the fine-particle content did not significantly modify the appearance of the body, whereas it markedly altered the composition of the front and its behavior. Reducing the fine fraction in the slurries induced a radical change of behavior for the front (see Figure 10.4):

- For muddy, fine-grained slurries, the front took the form of a blunt nose. Lack of slip along the flume bottom caused a conveyer-belt-like flow at the front.
- For coarse-grained slurries, the front took the form of a dry granular locked nose slipping along the bed as a result of the driving force exerted by the fluid accumulating behind the snout. Additional material was gradually incorporated into the snout, which grew in size until it was able to slow the body.

Interestingly enough, the changes in the rheological properties mainly affected the structure of the flow, especially within the tip region.

Iverson and his colleagues investigated slurries predominantly composed of a water-saturated mixture of sand and gravel, with a fine fraction of only a few percent (Iverson 1997, 2003a, 2005; Iverson et al. 2010). Experiments were run by releasing a volume of slurry (approximately 10 m^3) down a 31-degree, 95-m-long flume. At the base of the flume, the material spread out on a planar, nearly horizontal, unconfined runout zone. Flow-depth, basal normal stress, and basal interstitial-flow pressure were measured

at different places along the flume. Iverson and his co-workers observed that at early times (just after the release), an abrupt front formed at the head of the flow, which was followed by a gradually tapering body and a thin, more watery tail. The front remained relatively dry (with pressure of interstitial water dropping to zero) and of constant thickness, while the body elongated gradually in the course of the flow. Over the longest part of the flume, the basal pore pressure (i.e., the pressure of the interstitial water phase) nearly matched the total normal stress, which means that shear strength was close to zero and the material was liquefied within the body (Iverson 1997). In their recent data compilation, Iverson et al. (2010) confirmed the earlier observations made by Parsons et al. (2001): Mud enhanced flow mobility by maintaining high pore pressures in flow bodies. They also observed that roughness reduced flow speeds, but not runout distances. The explanation for this apparently strange behavior lies in the particular role played by debris agitation and grain-size segregation. Indeed, if the bed is flat, particles slip along the bottom, and shear is localized within a thin layer close to the bed, with almost no deformation through the flow depth (i.e., uniform velocity profile). In contrast, if the bed is corrugated, particles undergo collisions and are more agitated, which promotes the development of a nonuniform velocity profile through the depth and causes the flow to slightly dilate and the particles to segregate (see Section 10.4.3). Velocity shear and dilatancy act together as a sieve that constantly and randomly opens gaps. The finest particles are more likely to drop down into the gaps under the action of gravity than the coarsest ones are, which eventually creates inversely graded layers of particles (coarse particles on top, fine particle near the base of the flow). Here, particle segregation has two effects: (i) it reduces bottom friction (small particles acting as rolling balls) as shown in granular avalanche experiments carried out by (Phillips et al. 2006; Linares-Guerrero et al. 2007); (ii) the largest particles concentrate in the fast-moving upper layers (next to the free surface) and are transported to the flow front, where they are shouldered to the side by the core (made up of more mobile fine particles) and create static coarse-grained lateral levees that channelize the flow.

Figure 10.5 shows a sequence of aerial photographs taken when the material spread out on the runout surface. Self-organization of the slurry flow into a coarse-grained boundary and a muddy core became conspicuous as the flow traveled the runout surface. Lateral levees were formed by the coarsest grains that reached the front, being continuously shouldered aside by the muddy core. These levees then confined the ensuing muddy body. Note the levee formation is probably not induced by particle segregation alone since it is also observed for dry granular flows involving spherical equal-size particles (Félix and Thomas, 2004). Figure 10.6(a) shows the lateral levees, which can be used to evaluate the crosssection of the flow, and Figure 10.6(b) shows a granular levee formed by a debris flow on the alluvial fan. Similar features are also observed for wet-snow avalanches (Jomelli and Bertran 2001) and pyroclastic flows (Iverson and Vallance 2001).

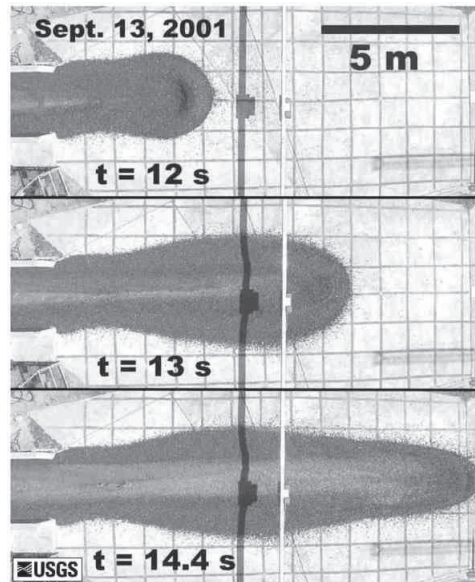


Figure 10.5. Snapshots showing slurry flow discharging from the U.S. Geological Survey Debris-Flow Flume and crossing the unconfined, nearly horizontal runout zone. The dark-toned material around the perimeter of the flow was predominantly gravel; the light-toned material in the center of the flow was liquified mud. Figure reproduced from Iverson (2003a); courtesy of Richard M. Iverson.

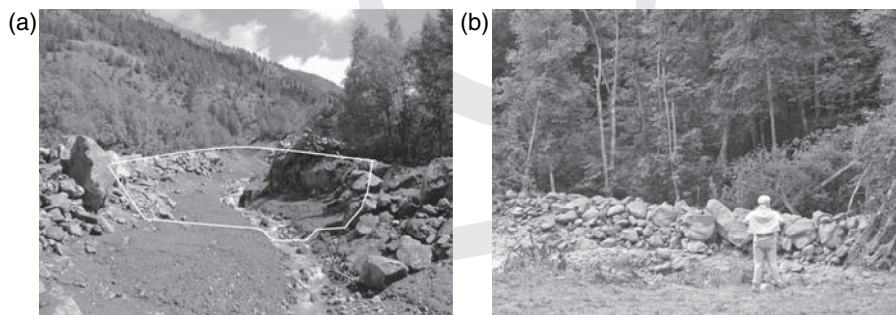


Figure 10.6. (a) Crosssection of the Malleval stream after a debris flow in August 1999 (Hautes-Alpes, France). (b) Levees left by a debris flow in the Dunant river in July 2006 (Valais, Switzerland); courtesy of Alain Delalune. For a color version of this figure please see the color plate section.

10.3.2 Anatomy of Powder-Snow Avalanches

Although there is probably no unique typical outline, powder-snow avalanches are usually made up of two regions when they are in a flowing regime (see Figure 10.7).

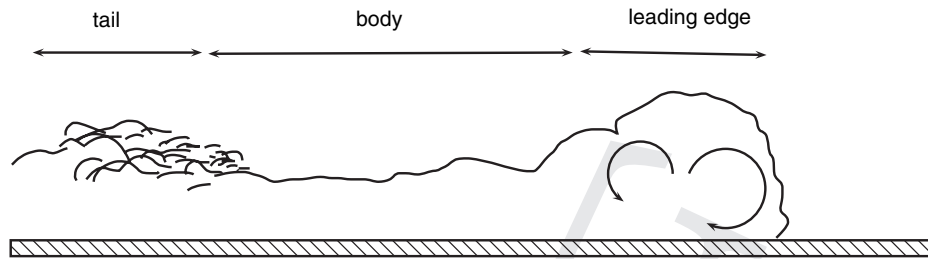


Figure 10.7. Anatomy of a powder-snow cloud.

- The leading edge is the frontal zone where intense mixing occurs. Motion is produced by the density contrast between the suspension and the surrounding fluid. Since the surrounding fluid is entrained into the current, the snow concentration decreases inside the current, leading, in turn, to a decrease in the buoyancy force unless the current is supplied by a sufficiently strong input of particles. Bed erosion and entrainment of the surrounding fluid into the head are therefore the two main processes that control the bulk dynamics. As long as this balance is maintained, the interface with the ambient fluid is a sharp surface that clearly delineates the avalanche and the ambient air. When air entrainment becomes the prevailing mechanism, the interface becomes a blurred layer. Turbulence is needed in the leading edge to counteract the particle settling; with sufficient turbulence, snow particles (ranging from snowflakes to snowballs) are maintained in suspension. The key condition for the formation and development of a powder cloud is that the vertical velocity fluctuations exceed the particle settling velocity, a condition that is reminiscent of the “ignition” of a gravity current on the ocean floor (Parker, 1982).
- The tail or “turbulent wake” is the volume of fluid behind the head, and it is often separated from the leading edge by a billow. The density contrast with the ambient fluid is usually much less marked than for the head. For some events, the powder-snow avalanche leaves behind a motionless cloud whose size may still be growing as a result of turbulent diffusion. It rapidly settles as turbulent energy falls off.

In the release and runout phase, the structure is usually very different. Indeed, in the release phase, the cloud is not formed (the avalanche looks like a flowing avalanche), whereas in the runout phase, the cloud collapses and settles to form a vast, thin deposit (thickness less than 1 m). For many events, it has been observed that the cloud separates from the dense core, which comes to a halt as soon as the slope gradient is too low (typically lower than 20–25%). This “decoupling” process is similar in many respects to the abrupt transition observed by Hallworth et al. (1998b) in their laboratory experiments on the instantaneous release of particle-driven gravity currents in a water-filled flume; it probably results from enhanced friction between particles, which implies higher dissipation rates in the core than in the dilute cloud. Figure 10.8a shows a powder-snow avalanche in a flowing regime. The trees on either side of the avalanche path give a scale of the depth of this avalanche. Its velocity was close to 60 m/s. Figure 10.8b also shows a powder-snow avalanche, but in its

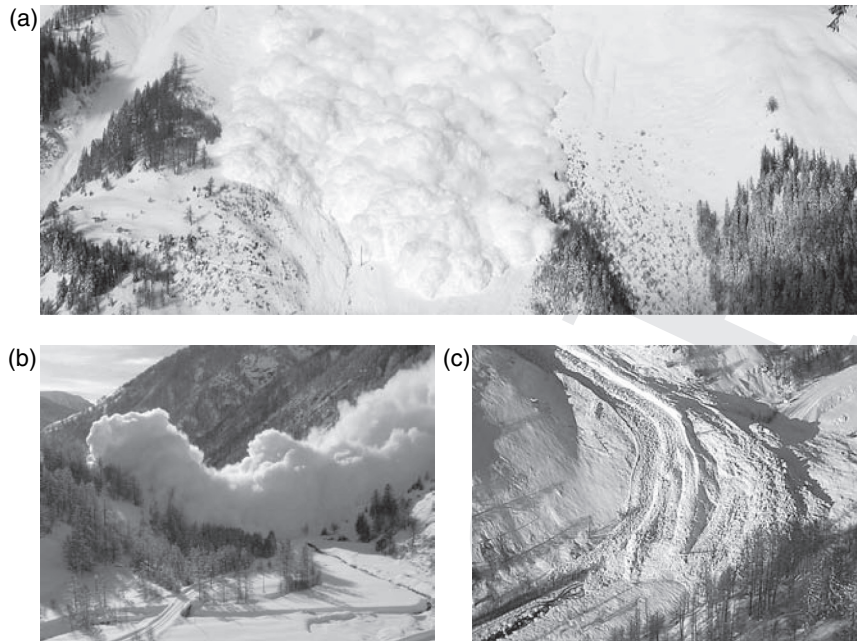


Figure 10.8. (a) Powder-snow avalanche in a flowing regime. Photograph taken in the Vallée-de-la-Sionne field site (Switzerland) in January 2004; courtesy of François Dufour, SLF. (b) Runup of a cloud of a powder-snow avalanche in a runout phase. Photograph taken at le Roux-d’Abriès, France in January 2004; courtesy of Maurice Chave. (c) Deposit of the dense core for the same avalanche; courtesy of Hervé Wadier. For a color version of this figure please see the color plate section.

runout phase. Note that the depth is much higher than the trees. Although its velocity was quite high, this cloud did not cause any damage to the forest, which implies that the impact pressure, and thus the bulk density, were low. Figure 10.8c shows that for this avalanche, part of the avalanche mass was concentrated in a dense core, which stopped prior to reaching the valley bottom.

There are not many field observations of the internal structure of powder-snow avalanches (Issler 2003; Rammer et al. 2007) and much of our current knowledge stems from what we can infer from small-scale experiments in the laboratory, which were conducted with a partial similitude with real flows. Field observations and laboratory experiments reveal the following four important aspects:

- *Existence of eddies:* Field measurements (based on radar or pressure-sensor measurements) show that the internal velocity is higher than the front velocity and varies cyclically with time, which was interpreted as the hallmark of rotational flows. Experiments of gravity currents in tanks have shown that the leading edge is associated with a pair of vortices, one located at the leading edge and another one at the rear of the head (see Figure 10.9). In experiments conducted by Simpson (1972), the development of the flow patterns was made visible using a blend of dense fluid and fine aluminum particles. A stretching vortex occupying the tip region

was clearly observed at the leading edge and produced an intense roll-up of fine aluminum particles, which makes it possible to visualize the streamlines and the two vortices; in the upper part of the head, a counterclockwise rotating vortex occurred. Experiments carried out by Ancey (2004) on finite-volume gravity currents moving down a slope also revealed that the particle cloud was composed of two evident eddies: when the surge involving a glass-bead suspension in water moved from left to right, he observed a small vortex ahead of the front, spinning clockwise, and a large counterclockwise eddy occupying most of the surge volume. Theoretically, this is in line with the paper of McElwaine (2005) who extended Benjamin's results by considering steady finite-volume currents flowing down a steep slope, which experience resistance from the surrounding fluid. Like Benjamin (1968), he found that the front makes a $\pi/3$ angle with the bottom line. More recently, Ancey et al. (2006; 2007) worked out analytical solutions to the depth-averaged equations and the Euler equations, which represent the flow of non-Boussinesq currents; it was also found that the flow must be rotational and that the head is wedge-shaped.

- *Vertical density stratification*: Turbulence is often not sufficient to mix the cloud efficiently and maintain a uniform density through the cloud depth. Instead, a dense layer forms at the bottom and the density decreases quickly upward (Issler 2003). For many events, it has also been observed that the dilute component of the avalanche flowed faster than the core and eventually detached from it, which leads us to think that there was a sharp transition from the dense basal layer to the dilute upper layer. For instance, from impact force measurement against static obstacles, it was inferred that the dense layer at the base of the flow was 1–3 m thick, with velocity and (instantaneous) impact pressure as high as 30 m/s and 400 kPa. The transition layer is typically 5 m thick, with kinetic pressure in the 50–100 kPa range. In the dilute upper layer, which can be very thick (as large as 100 m), the kinetic pressure drops to a few pascals, but the velocity is quite high, with typical values close to 60–80 m/s.
- *Snow entrainment*: It alters speed and runout distance. The primary mode of entrainment appeared to be frontal ploughing, although entrainment behind the avalanche front was also observed (Gauer and Issler 2003; Sovilla and Bartelt 2006). When there is snow entrainment, the front is wedge shaped. It can present lobes and clefts, more occasionally fingering patterns, which appear and quickly disappear. The total flow depth lies in the 10–50 m range and varies little with distance. Theoretical calculations predict a wedge angle of $\pi/3$, which seems consistent with field observations (McElwaine 2005). In the absence of entrainment, the front becomes vertical, with a typical nose shape. The surface is diffuse and smoother. The flow depth can be as large as 100 m and quickly varies with distance.
- *Air entrainment*: Changes in cloud volume result primarily from the entrainment of the surrounding air. Various mixing processes are responsible for the entrainment of an ambient, less-dense fluid into a denser current (or cloud). It has been shown for jets, plumes, and currents that (1) different shear instabilities (Kelvin-Helmoltz, Hölmböe, etc.) can occur at the interface between dense and less dense fluids, and (2) the rate of growth of these instabilities is controlled by a Richardson number (Turner 1973; Fernando 1991), defined here as

$$Ri = \frac{g' H \cos \theta}{U^2}, \quad (10.1)$$

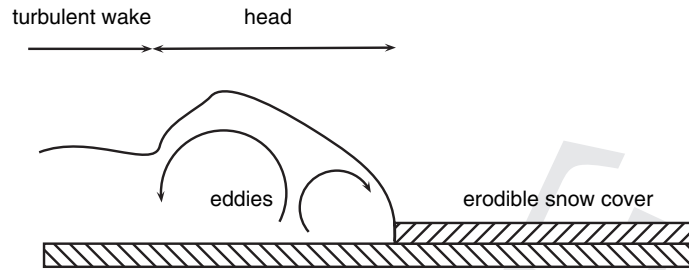


Figure 10.9. Typical structure of the head of a powder-snow avalanche as interpreted from field measurements and laboratory experiments.

where g' denotes the reduced gravity $g' = g\Delta\bar{\rho}/\rho_a$ and $\Delta\bar{\rho} = \bar{\rho} - \rho_a$ is the density mismatch between the cloud and the ambient fluid. Note that the Richardson number is the inverse square of the Froude number used in hydraulics. The Richardson number can be seen as the ratio of the potential energy ($g\Delta\bar{\rho}H\cos\theta$) to the kinetic energy ($\rho_a U^2$) of a parcel of fluid at the current interface. Usually a smaller Ri value implies predominance of inertia effects over the restoring action of gravity, thus resulting in greater instability and therefore a higher entrainment rate; it is then expected that the entrainment rate is a decreasing function of the Richardson number. Mixing is observed to occur in gravity currents due to the formation of Kelvin-Helmoltz instabilities at the front, which grow in size, are advected upward, and finally collapse behind the head. The lobe-and-cleft instability is also an efficient mechanism of entrainment (Simpson 1997). Although the details of the mixing mechanisms are very complex, a striking result of recent research is that their overall effects can be described using simple relations with bulk variables (Turner 1973; Fernando 1991). For instance, as regards the volume balance equation, the most common assumption is to state that the volume variations result from the entrainment of the ambient fluid into the cloud and that the inflow rate is proportional to the exposed surface areas and a characteristic velocity u_e : $\dot{V} = E_v S u_e$ where E_v is the bulk entrainment coefficient and $u_e = \sqrt{\bar{\rho}/\rho_a} U$ for a non-Boussinesq current.

10.4 Fluid-Mechanics Approach to Gravity Currents

Gravity-driven flows usually take the appearance of more or less viscous fluids flowing down a slope, and this observation has prompted the use of fluid-mechanics tools for describing their motion. However, the impediments to a full fluid-mechanics approach are many: a wide range of particle size (often in the 10^{-3} –1-m range), composition that may change with time and/or position, poorly known boundary conditions (e.g., erodible basal surface) and initial conditions, time-dependent flows with abrupt changes (e.g., surge front, instabilities along the free surface), and so on. All these difficulties pose great challenges in any fluid-mechanics approach for modeling rapid mass movements and have given impetus to extensive research combining laboratory and field experiments, theory, field observation, and numerical simulations.

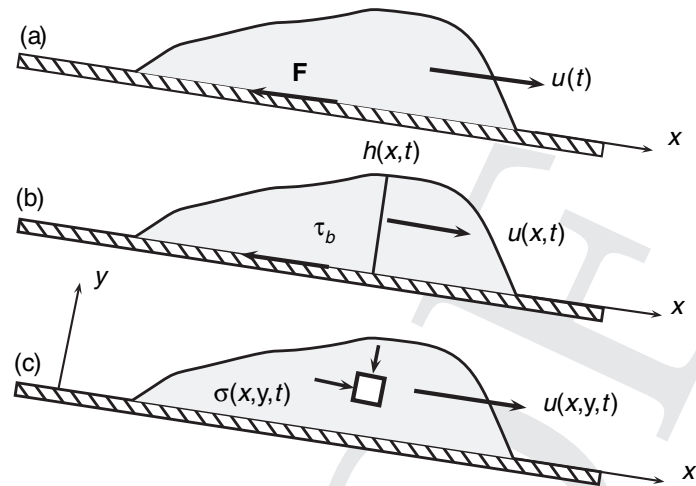


Figure 10.10. Different spatial scales used for describing avalanches (and related flows): (a) the avalanche as a rigid body moving at velocity $\mathbf{u}(t)$; (b) the avalanche as a stream of depth $h(x, t)$ and velocity $\mathbf{u}(x, t)$; (c) the avalanche as a continuum.

Avalanches and debris flows can be considered at different spatial scales (see Figure 10.10). The larger scale, corresponding to the entire flow, leads to the simplest models. The chief parameters include the location of the gravity center and its velocity. Mechanical behavior is mainly reflected by the friction force F exerted by the bottom (ground or snowpack) on the avalanche. The smallest scale, close to the size of snow particles involved in the avalanches, leads to complicated rheological and numerical problems. The flow characteristics (velocity, stress) are calculated at any point of the occupied space. Intermediate models have also been developed. These models benefit from being less complex than three-dimensional numerical models and yet are more accurate than simple ones. Such intermediate models are generally obtained by integrating the equations of motion through the flow depth, as is done in hydraulics for shallow water equations.

We start our review of these three approaches with a discussion of the flow regimes (see Section 10.4.1). We then briefly describe the rheological behavior of natural materials involved in gravity flows in Section 10.4.2. Since most gravity flows are made up of different sized particles, the rheological properties usually on the solids concentration of each component. As a result of various processes such as kinetic sieving, particles can migrate and segregate. In Section 10.4.3, we tackle the difficult issue of particle segregation. The second part of this section is devoted to presenting three fluid-mechanics approaches. In Section 10.4.4, we outline the simplest approach: the sliding-block model, which can be used to give some crude estimates of the speed and dynamic features as well as scaling relations between flow variables and input parameters. A more involved approach consists of taking the depth average of the local governing equations (see Section 10.4.5), which enables us to derive a set of

partial differential equations for the flow depth h and mean velocity \bar{u} . In principle, the local governing equations could be integrated numerically, but the numerical cost is very high and the gain in accuracy is spoiled by the poor knowledge of the rheologic properties or the initial/boundary conditions. Here we confine attention to analytical treatments, which involves working out approximate solutions by using asymptotic expansions of the velocity field (see Section 10.4.6).

10.4.1 Scaling and Flow Regimes

Here we will examine how different flow regimes can occur depending on the relative strength of inertial, pressure, and viscous contributions in the governing equations. Dimensional analysis helps clarify the notions of *inertia-dominated* and *friction-dominated* regimes. In the analytical computations, we will use the shallowness of flows to derive approximate equations.

We consider a shallow layer of fluid flowing over a rigid impermeable plane inclined at an angle θ (see Figure 10.11). The fluid is incompressible; its density is denoted by ρ and its bulk viscosity by $\eta = \tau/\dot{\gamma}$, with $\dot{\gamma}$ the shear rate (i.e., in a simple shear flow, it is the velocity gradient in the y -direction). Note that this bulk viscosity may depend on $\dot{\gamma}$ (this is the general case when the behavior is non-Newtonian). The ratio $\epsilon = H_*/L_*$ between the typical vertical and horizontal length scales, H_* and L_* , respectively, is assumed to be small. The streamwise and vertical coordinates are denoted by x and y , respectively.

A two-dimensional flow regime is assumed (i.e., any cross-stream variation is neglected). The depth of the layer is given by $h(x, t)$. The horizontal and vertical velocity components of the velocity \mathbf{u} are denoted by u and v , respectively. The pressure is referred to as $p(x, y, t)$, where t denotes time, whereas the extra stress tensor (or deviatoric stress tensor) is denoted by $\boldsymbol{\sigma}$. The surrounding fluid (assumed to be air) is assumed to be dynamically passive (i.e., inviscid and low density compared to the

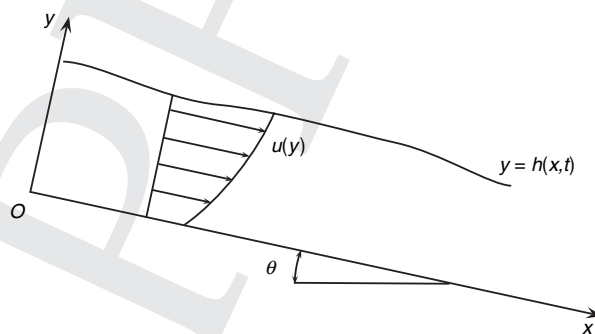


Figure 10.11. The configuration of the flow: $h(x, t)$ the flow depth, $u(y)$ the cross-stream velocity profile, and θ the bed inclination.

moving fluid) and surface tension is neglected, which implies that the stress state at the free surface is zero.

The governing equations are given by the mass and momentum balance equations

$$\nabla \cdot \mathbf{u} = 0, \quad (10.2)$$

$$\rho \frac{\partial \mathbf{u}}{\partial t} + \rho(\mathbf{u} \cdot \nabla) \mathbf{u} = \rho \mathbf{g} - \nabla p + \nabla \cdot \boldsymbol{\sigma}, \quad (10.3)$$

supplemented by the following boundary conditions at the free and bottom surfaces

$$v(x, h, t) = \frac{dh}{dt} = \frac{\partial h}{\partial t} + u(x, h, t) \frac{\partial h}{\partial x}, \quad v(x, 0, t) = 0. \quad (10.4)$$

There are many ways of transforming these governing equations into dimensionless expressions (Liu and Mei 1990a; Balmforth and Craster 1999; Keller 2003; Ancey and Cochard 2009). Here we depart slightly from the presentation given by Liu and Mei (1990a). The characteristic streamwise and vertical velocities, the timescale, the typical pressure, and the order of magnitude of bulk viscosity are referred to as U_* , V_* , T_* , P_* , and η_* , respectively. Moreover, in addition to the lengthscale ratio ϵ , we introduce the following dimensionless numbers that characterize free-surface, gravity-driven flows: the flow Reynolds number and the Froude number

$$\text{Re} = \frac{\rho U_* H_*}{\eta_*} \quad \text{and} \quad \text{Fr} = \frac{U_*}{\sqrt{g H_* \cos \theta}}.$$

The following dimensionless variables will be used in this section:

$$\hat{u} = \frac{u}{U_*}, \quad \hat{v} = \frac{v}{V_*}, \quad \hat{x} = \frac{x}{L_*}, \quad \hat{y} = \frac{y}{H_*}, \quad \text{and} \quad \hat{t} = \frac{t}{T_*}.$$

A natural choice for T_* is $T_* = L_*/U_*$. The stresses are scaled as follows:

$$\hat{\sigma}_{xx} = \frac{\eta_* U_*}{L_*} \sigma_{xx}, \quad \hat{\sigma}_{xy} = \frac{\eta_* U_*}{H_*} \sigma_{xy}, \quad \hat{\sigma}_{yy} = \frac{\eta_* U_*}{L_*} \sigma_{yy}, \quad \text{and} \quad \hat{p} = \frac{p}{P_*},$$

where σ_{xx} , σ_{xy} , and σ_{yy} are the normal stress in the x -direction, the shear stress, and the normal stress in the y -direction, respectively. Here we are interested in free-surface flows. This leads us to set $P_* = \rho g H_* \cos \theta$ since we expect that, to leading order, the pressure adopts a hydrostatic distribution (see later). If we define the vertical velocity scale as $V_* = \epsilon U_*$, the mass balance equation (10.2) takes the following dimensionless form

$$\frac{\partial \hat{u}}{\partial \hat{x}} + \frac{\partial \hat{v}}{\partial \hat{y}} = 0. \quad (10.5)$$

Substituting the dimensionless variables into the momentum balance equation (10.3) leads to

$$\epsilon \text{Re} \frac{d\hat{u}}{d\hat{t}} = \frac{\epsilon \text{Re}}{\text{Fr}^2} \left(\frac{1}{\epsilon} \tan \theta - \frac{\partial \hat{p}}{\partial \hat{x}} \right) + \epsilon^2 \frac{\partial \hat{\sigma}_{xx}}{\partial \hat{x}} + \frac{\partial \hat{\sigma}_{xy}}{\partial \hat{y}}, \quad (10.6)$$

$$\epsilon^3 \text{Re} \frac{d\hat{v}}{d\hat{t}} = \frac{\epsilon \text{Re}}{\text{Fr}^2} \left(-1 - \frac{\partial \hat{p}}{\partial \hat{y}} \right) + \epsilon^2 \frac{\partial \hat{\sigma}_{xy}}{\partial \hat{x}} + \epsilon^2 \frac{\partial \hat{\sigma}_{yy}}{\partial \hat{y}}. \quad (10.7)$$

The momentum balance equation expresses a balance between gravity acceleration, inertial terms, pressure gradient, and viscous dissipation, whose order of magnitude is $\rho g \sin \theta$, $\rho U_*^2/L_*$, P_*/L_* , and $\eta_* U_*/H_*^2$, respectively. Depending on the values considered for the characteristic scales, different types of flow regime occur. At least four regimes, where two contributions prevail, could be achieved in principle:

1. *Inertial regime*, where inertial and pressure-gradient terms are of the same magnitude. We obtain

$$U_* = \sqrt{g H_* \cos \theta}.$$

The order of magnitude of the shear stress is $\partial \sigma_{xy}/\partial y = \rho g O(\epsilon^{-1} \text{Re}^{-1})$. This regime occurs when $\epsilon \text{Re} \gg 1$ and $\text{Fr} = O(1)$.

2. *Diffusive regime*, where the pressure gradient is balanced by viscous stresses within the bulk. In that case, we have

$$U_* = \frac{\rho g \cos \theta H_*^3}{\eta_* L_*}.$$

Inertial terms must be low compared to the pressure gradient and the slope must be shallow ($\tan \theta \ll \epsilon$). This imposes the following constraint: $\epsilon \text{Re} \ll 1$. We deduced that $\text{Fr}^2 = O(\epsilon \text{Re}) \ll 1$.

3. *Visco-inertial regime*, where inertial and viscous contributions are nearly equal. In that case, we have

$$U_* = \frac{1}{\epsilon} \frac{\eta_*}{\rho H_*}.$$

The pressure gradient must be low compared to the viscous stress, which entails the following condition: $\eta_* \gg \epsilon \rho \sqrt{g H_*^3}$. We obtain $\epsilon \text{Re} \sim 1$ and $\text{Fr} = \eta_*/(\rho \epsilon \sqrt{g H_*^3}) \gg 1$.

4. *Nearly steady uniform regime*, where the viscous contribution matches gravity acceleration. In that case, we have

$$U_* = \frac{\rho g \sin \theta H_*^2}{\eta_*}.$$

Inertia must be negligible, which means $\epsilon \ll 1$ (stretched flows). We obtain $\text{Re} = O(\text{Fr}^2)$ and $\tan \theta \gg \epsilon$ (mild slopes).

In the *inertia-dominated regime*, the rheological effects are so low that they can be neglected and the final governing equations are the Euler equations; this approximation can be used to describe high-speed flows such as powder-snow avalanches in the flowing regime (Ancy et al. 2007). The *visco-inertial regime* is more spurious and has no specific interest in geophysics, notably because the flows are rapidly unstable. More interesting is the *diffusive regime* that may be achieved for very slow flows on gentle slopes ($\theta \ll 1$), typically when flows come to rest, or within the head (Liu and Mei 1990b; Balmforth et al. 2002; Ancy and Cocharde 2009; Ancy et al. 2009). We will further describe this regime in Section 10.5.3. The *nearly-steady regime*

will be exemplified in Section 10.5.2 within the framework of the kinematic-wave approximation.

Note that the partitioning into four regimes holds for viscous (Newtonian) fluids and non-Newtonian materials for which the bulk viscosity does not vary significantly with shear rate over a sufficiently wide range of shear rates. In the converse case, further dimensionless groups (e.g., the Bingham number) must be introduced, which makes this classification more complicated.

10.4.2 Rheology

In geophysical fluid mechanics, there have been many attempts to describe the rheological behavior of natural materials (Ancey 2007). However, since rheometric experiments are not easy (see later), scientists use proxy procedures to characterize the rheological behavior of natural materials. Interpreting the traces of past events (e.g., shape of deposits), running small-scale experiments with materials mimicking the behavior of natural materials, and making analogies with idealized materials are common approaches to this issue. Because of a lack of experimental validation, there are many points of contention within the different communities working on geophysical flows. A typical example is provided by the debate surrounding the most appropriate constitutive equation for describing sediment mixtures mobilized by debris flows (Iverson 2003a). A certain part of the debris flow community uses soil-mechanics concepts (Coulomb behavior), whereas another part prefers viscoplastic models. A third part of the community merges the different concepts from soil and fluid mechanics to provide general constitutive equations.

Over the last 20 years, a large number of experiments have been carried out to test the rheological properties of natural materials. The crux of the difficulty lies in the design of specific rheometers compatible with the relatively large size of particles involved in geophysical flows. Coaxial-cylinder (Couette) rheometers and inclined flumes are the most popular geometries. Another source of trouble stems from additional effects such as particle migration and segregation, flow heterogeneities, fracture, layering, etc. These effects are often very pronounced with natural materials, which may explain the poor reproducibility of rheometric investigations (Major and Pierson 1992; Contreras and Davies 2000; Iverson 2003b). Poor reproducibility, complexity in the material response, and data scattering have at times been interpreted as the failure of the one-phase approximation for describing rheological properties (Iverson, 2003b). In fact, these experimental problems demonstrate above all that the bulk behavior of natural material is characterized by fluctuations that can be as wide as the mean values. As for turbulence and Brownian motion, we should describe not only the mean behavior, but also the fluctuating behavior to properly characterize the rheological properties. For concentrated colloidal or granular materials (Lootens et al. 2003; Tsai et al. 2001), experiments on well-controlled materials have provided evidence

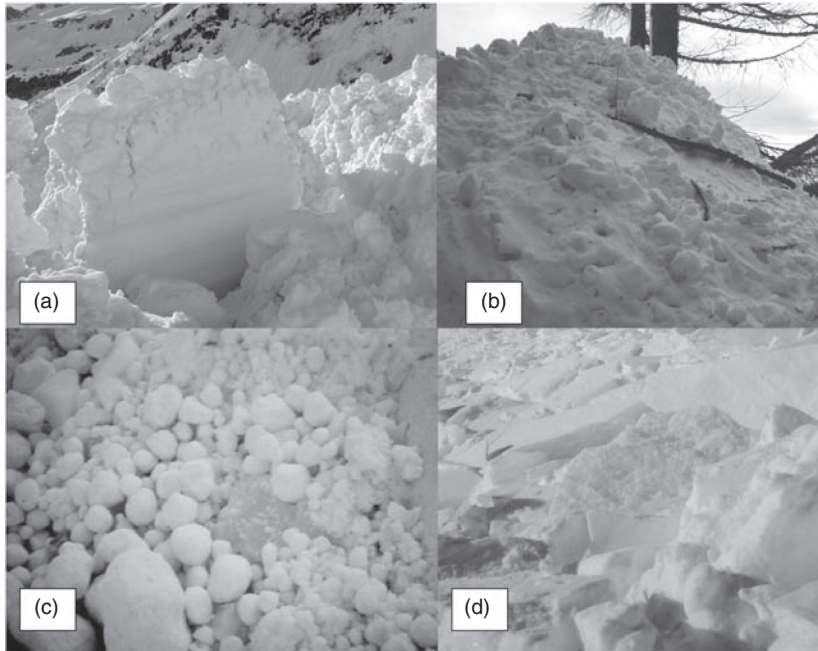


Figure 10.12. Different types of snow observed in avalanche deposits. (a) Block of wet snow (size: 1 m). (b) Slurry of dry snow including weak snowballs formed during the course of the avalanche (the heap height was approximately 2 m). (c) Ice balls involved in a huge avalanche coming from the north face of the Mont Blanc (France); the typical diameter was 10 cm. (d) Sintered snow forming broken slabs (typical length: 40 cm, typical thickness 10 cm). For a color version of this figure please see the color plate section.

that to some extent; these fluctuations originate from jamming in the particle network (creation of force vaults sustaining normal stress and resisting against shear stress, both of which suddenly relax). Other processes such as ordering, aging (changes in the rheological behavior over time as a result of irreversible processes), and chemical alteration occur in natural slurries, which may explain their time-dependent properties (Marquez et al., 2006). Finally, there are perturbing effects (e.g., slipping along the smooth surfaces of a rheometer) that may bias measurement.

Snow is a very special material. To illustrate the diversity of materials involved in snow avalanches, Figure 10.12 reports different types of snow observed in avalanche deposits. Experiments have been done in the laboratory to characterize snow's rheological behavior. Authors such as Dent and Lang (1982) and Maeno (1993) have measured the velocity profile within snow flows and generally deduced that snow generates a non-Newtonian viscoplastic flow whose properties depend a great deal on density. Carrying these laboratory results over to real avalanches is not clearly reliable because of size-scale effects and similarity conditions. Furthermore, given the severe difficulties inherent in snow rheometry (sample fracture during shearing tests,

variation in the snow microstructure resulting from thermodynamic transformations of crystals, etc.), properly identifying the constitutive equation of snow with modern rheometers is out of reach for the moment. More recently, Ancey and Meunier (2004) showed how avalanche-velocity records can be used to determine the bulk frictional force; a striking result is that the bulk behavior of most snow avalanches can be approximated using a Coulomb frictional model. Kern (2004; 2009) ran outdoor experiments to measure shear-rate profiles inside snow flows to infer rheological properties; this preliminary experiment is rather encouraging and clears the way for precise rheometrical investigations of real snow avalanches.

Since little sound field or laboratory data are available on the basic rheological processes involved in avalanche release and flow, all avalanche-dynamics models proposed so far rely on analogy with other physical phenomena: typical examples include analogies with granular flows (Savage and Hutter 1989; Savage 1989; Tai et al. 2001; Cui et al. 2007), Newtonian fluids (Hunt 1994), power-law fluids (Norem et al. 1986), and viscoplastic flows (Dent and Lang 1982; Ancey 2007). From a rheological point of view, these models rely on a purely speculative foundation. Indeed, most of the time, the rheological parameters used in these models have been estimated by matching the model predictions (such as the leading-edge velocity and the runout distance) with field data (Buser and Frutiger 1980; Dent and Lang 1980; Ancey et al. 2004). However, this procedure obviously does not provide evidence that the constitutive equation is appropriate.

For debris flows, natural suspensions are made up of a great diversity of grains and fluids. This observation motivates fundamental questions: How do we distinguish between the solid and fluid phases? What is the effect of colloidal particles in a suspension composed of coarse and fine particles? When the particle size distribution is bimodal (i.e. we can distinguish between fine and coarse particles), the fine fraction and the interstitial fluid form a viscoplastic fluid embedding the coarse particles, as suggested by Sengun and Probst (1989); this leads to a wide range of viscoplastic constitutive equations, the most common being the Herschel-Bulkley model, described later. The bimodal-suspension approximation usually breaks for poorly sorted slurries. In that case, following Iverson and his co-workers (Iverson 1997; 2005), Coulomb plasticity can help understand the complex, time-dependent rheological behavior of slurries.

When the bulk is made up of fine colloidal particles, phenomenological laws are used to describe rheological behavior. One of the most popular is the Herschel-Bulkley model, which generalizes the Bingham law

$$\tau = \tau_c + K \dot{\gamma}^n, \quad (10.8)$$

with τ_c the yield stress and K and n two constitutive parameters; the linear case ($n = 1$) is referred to as the Bingham law. In practice, this phenomenological expression successfully describes the rheological behavior of many materials over a sufficiently wide range of shear rates, except at very low shear rates.

When the bulk is made up of coarse noncolloidal particles, Coulomb friction at the particle level imparts its key properties to the bulk, which explains (i) the linear relationship between the shear stress τ and the effective normal stress $\sigma' = \sigma - p$ (with p the interstitial pore pressure, σ the stress normal to the plane of shearing)

$$\tau = \sigma' \tan \varphi, \quad (10.9)$$

and (ii) the nondependence of the shear stress on the shear rate $\dot{\gamma}$. Some authors have suggested that in high-velocity flows, particles undergo collisions, which gives rise to a regime referred to as the frictional-collisional regime. The first proposition of bulk stress tensor seems to be attributable to Savage (1982), who split the shear stress into frictional and collisional contributions

$$\tau = \sigma \tan \varphi + \mu(T)\dot{\gamma}, \quad (10.10)$$

with T the granular temperature (root mean square of grain velocity fluctuations). Elaborating on this model, Ancey and Evesque (2000) suggested that there is a coupling between frictional and collisional processes. Using heuristic arguments on energy balance, they concluded that the collisional viscosity should depend on the Coulomb number $\text{Co} = \rho_p a^2 \dot{\gamma}^2 / \sigma$ (with a the particle radius and ρ_p its density) to allow for this coupling in a simple way

$$\tau = \sigma \tan \varphi + \mu(\text{Co})\dot{\gamma}. \quad (10.11)$$

Jop et al. (2005) proposed a slightly different version of this model, where both the bulk frictional and collisional contributions collapse into a single term, which is a function of the inertial number $I = \text{Co}^{1/2}$ (i.e., a variant of Coulomb number)

$$\tau = \sigma \tan \varphi(I). \quad (10.12)$$

In contrast, Josserand et al. (2004) stated that the key variable in shear stress was the solid concentration ϕ rather than the Coulomb number

$$\tau = K(\phi)\sigma + \mu(\phi)\dot{\gamma}^2, \quad (10.13)$$

with K a friction coefficient. Every model is successful in predicting experimental observations for some flow conditions, but to date, none is able to describe the frictional-collisional regime for a wide range of flow conditions and material properties.

10.4.3 Segregation and Particle Migration

Particle segregation refers to a sorting process that leads to separating a mixture containing free-flowing particles, the size distribution of which is sufficiently wide (at least a factor of 2 between the finest and coarsest grain sizes). It is an important feature of sheared granular flows, in which the coarsest particles rise to the top of the flow,

while the finest percolate down to the bottom. By changing the local composition of the bulk, segregation has significant consequences on the behavior of granular avalanches made up of different-sized particles, for example, by increasing their runout distance (Legros 2002; Linares-Guerrero et al. 2007), forming bouldery fronts (Gray and Kokelaar 2010), and giving rise to segregation-mobility feedback effects (Gray and Ancey 2009). While the effects of particle segregation on bulk dynamics has been essentially investigated in the laboratory, there is substantial field evidence that segregation is a key mechanism in natural gravity flows such as snow avalanches (Bartelt and McArdell 2009) and debris flows (Iverson and Vallance 2001).

Among the numerous processes that cause segregation, kinetic sieving and squeeze expulsion are likely to be the most efficient in dense, dry, granular flows down sloping beds (Gray 2010): Velocity shear and dilatancy act together as a random fluctuating sieve that allows the finer particles to percolate to the bottom under the action of gravity, while squeezing larger particles upward. Figure 10.13 shows a typical experiment of particle segregation in a granular flow down a chute: Small beads were injected from above while large particles crept along the flume base. The small particles rapidly percolated to the bottom, whereas the large ones drifted to the top of the flow.

Segregation in dense granular flows has been investigated theoretically using different approaches, including information entropy theory, statistical mechanics, and binary-mixture theory (Gray 2010; Ottino and Khakhar 2000). For dense granular flows involving binary mixtures, the last theoretical approach is interesting in that it provides a relatively simple description of segregation-remixing in the form of a nonlinear advection diffusion equation for the concentration (Gray 2010):

$$\frac{\partial \phi}{\partial t} + \text{div}(\phi \mathbf{u}) - \frac{\partial}{\partial z} \left(q \phi (1 - \phi) \right) = \frac{\partial}{\partial z} \left(D \frac{\partial \phi}{\partial z} \right), \quad (10.14)$$

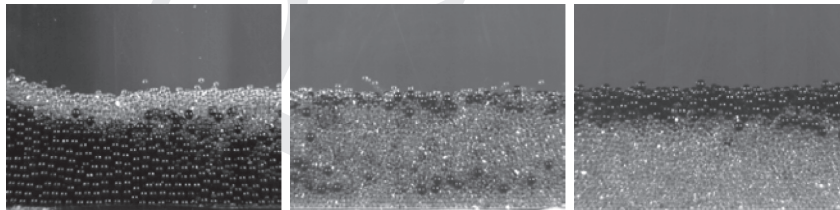


Figure 10.13. Snapshots showing particles segregating down a flume. Initially, when the particles enter the chute (image on the left), the mixture is normally graded, with all the small particles (1-mm-diameter glass beads, colored) on top of the coarse grains (2-mm-diameter glass beads in black). Segregation leads to a grading inversion, in which the smallest particles percolate to the bottom of the flow, while the largest rise toward the free surface (image in the middle). In the final state (in this experiment, approximately 1 m downward of the flume entrance), the particles separate out, with the large particles on top and small particles next to the bottom (image on the right).

where ϕ is the small particle concentration ($1 - \phi$ is then the concentration in large particles), \mathbf{u} is the bulk velocity field, D is a coefficient of diffusion, and q is the percolation rate (i.e., the rate at which small particles percolate to the base). The first term on the left-hand side of (10.14) is the time rate of change of the small particle concentration, and the second term is due to advection by the bulk velocity field \mathbf{u} . The third nonlinear term accounts for segregation, while the right-hand side introduces the diffusive effects of remixing. Mathematically, this equation is a second-order parabolic equation when $D > 0$. For $D = 0$, it reduces to a hyperbolic first-order partial differential equation and in this case, equation (10.14) may form shocks (i.e., waves across which the small particle concentration experiences a jump). When $D > 0$, diffusive remixing smears out the shock wave, replacing it by a smooth transition in the small-particle concentration, and equation (10.14) is then able to model experiments very realistically, but for practical purposes, neglecting the remixing (thus assuming $D = 0$) simplifies a great deal equation (10.14), which is then more amenable to analysis (Gray and Kokelaar 2010). This situation is reminiscent of water flows, in which sharp gradients in flow depth are replaced by discontinuities called *hydraulic jumps* (LeVeque 2002). Equation (10.14) does not depend on a particular form of governing equations for the bulk, and it is therefore compatible with most existing granular-flow models.

Particle migration refers to the diffusion of particles in sheared flows of particle suspensions, which produces inhomogeneous particle concentrations through the suspension (Stickel and Powell 2005). In a simple shear flow, the particles are driven toward the regions that are characterized by low shear rates, whereas regions dominated by high shear rates tend to become free of particles. For concentrated suspensions of particles in a viscous fluid, this diffusion process markedly affects the flow dynamics since the bulk viscosity μ depends on the particle concentration ϕ , a dependence that is well captured by the empirical Krieger-Dougherty equation

$$\mu = \mu_0 \left(1 - \frac{\phi}{\phi_m} \right)^{-\frac{5}{2}\phi_m},$$

where ϕ_m is the maximum packing fraction and μ_0 is the viscosity of the interstitial fluid (Chang and Powell 1994; Stickel and Powell 2005; Morris 2009). This change in the local rheological properties has profound impact on the bulk properties by giving rise to non-Newtonian properties such as normal-stress effects and apparent yield stress (Zarraga et al. 2000; Ovarlez et al. 2006). For suspension flows down sloping beds, particle migration causes the particles to rise to the free surface of the flow (Singh et al. 2006; Timberlake and Morrison 2005). The upper layers next to the free surface move faster and accumulate particles, which tend to be transported to the flow front, forming pasty flow fronts. This situation is reminiscent of the observations made by Parsons et al. (2001) (see Figure 10.4).

The time variations in the particle concentration are described by an advection diffusion equation

$$\frac{\partial \phi}{\partial t} + \langle \mathbf{u} \rangle \cdot \nabla \phi = -\nabla \cdot \mathbf{j}, \quad (10.15)$$

where $\mathbf{j} = \phi(\langle \mathbf{u} \rangle_p - \langle \mathbf{u} \rangle)$ denotes the particle flux (relative to the bulk flow), $\langle \mathbf{u} \rangle$ is the average bulk velocity field, and $\langle \mathbf{u} \rangle_p$ is the average particle velocity. As with other diffusion processes, particle migration has been modeled by relating the particle flux \mathbf{j} to a driving force or potential. Since it was observed that particles migrate from regions of high to low shear rate, the first phenomenological law proposed by Leighton and Acrivos (1987) was to assume that $\mathbf{j} \propto -\dot{\gamma}$, with $\dot{\gamma}$ the shear rate. A more general formulation was then proposed by Morris and Boulay (1999), who showed using microstructural arguments that

$$\mathbf{j} \propto \nabla \cdot \langle \boldsymbol{\Sigma} \rangle_p,$$

where $\langle \boldsymbol{\Sigma} \rangle_p$ denotes the average particle stress tensor. This law performs fairly well for a number of flow configurations (Morris 2009).

10.4.4 Sliding-Block and Box Models

The simplest model for computing the propagation speed of a gravity current proceeds by assuming that there is no downstream variation in flow properties (i.e., density, friction) within the flowing bulk. Several classes of models have been developed.

- *Sliding block model*: The flow is assumed to behave as a rigid block experiencing a frictional force. The early models date back to the beginning of the 20th century (Mougin 1922). Similar models have been developed for debris flows (Zimmermann et al. 1997). See Section 10.5.1.
- *Box model*: The model relaxes the rigidity assumption of the sliding block model by considering that the current behaves as a deformable rectangular box of length ℓ and height h (Hogg et al. 2000; Ungarisch 2009). Mass conservation implies that the volume of this rectangle is known. For inertia-dominated flows, the Froude number at the leading edge is usually given by a boundary condition such as the von Kármán condition: $Fr = u_f / \sqrt{g'h} = \text{constant}$ (with g' the reduced gravity acceleration, see (10.1), and u_f the front velocity). Since box models have been developed for flows on horizontal surface, they are not well suited to studying flows on steep slope.
- *Cloud model*: The current is assumed to behave as a deformable body whose shape keeps the same aspect. The governing equations are given by the mass and momentum conservation equations for a mass-varying body (Kulikovskiy and Svehnikova, 1977). See Section 10.6.1.

For almost 80 years, simple models have been developed to provide crude estimations of avalanche features (velocity, pressure, runout distance). They are extensively used in engineering throughout the world. Despite their simplicity and approximate

character, they can provide valuable results (Bozhinskiy and Losev 1998; Salm 2004; Ancey 2005).

10.4.5 Depth-Averaged Equations

The most common method for solving free-surface problems is to take the depth-average of the local equations of motion. In the literature, this method is referred to as the Saint-Venant approach since it was originally developed to compute floods in rivers.

We consider flows without entrainment of the surrounding fluid and without variation in density (see Section 10.6.2 for flow with entrainment). Accordingly, the bulk density may be merely replaced by its mean value. In this context, the equations of motion may be inferred in a way similar to the usual procedure used in hydraulics to derive the shallow water equations (or Saint-Venant equations). It involves integrating the momentum and mass balance equations over the depth. As such, a method has been extensively used in hydraulics for water flow (Chow 1959) as well for non-Newtonian fluids (Savage and Hutter 1991; Bouchut et al. 2003), we briefly recall the principle and then directly provide the resulting equations of motion. Let us consider the local mass balance: $\partial \rho / \partial t + \nabla \cdot (\rho \mathbf{u}) = 0$. Integrating this equation over the flow depth leads to

$$\int_0^{h(x,t)} \left(\frac{\partial u}{\partial x} + \frac{\partial v}{\partial y} \right) dy = \frac{\partial}{\partial x} \int_0^h u(x, y, t) dy - u(h) \frac{\partial h}{\partial x} + v(x, h, t) - v(x, 0, t), \quad (10.16)$$

where u and v denote the x - and y -component of the local velocity. At the free surface and at the bottom, the y -component of velocity satisfies the following boundary conditions:

$$v(x, h, t) = \frac{dh}{dt} = \frac{\partial h}{\partial t} + u(x, h, t) \frac{\partial h}{\partial x}, \quad (10.17)$$

$$v(x, 0, t) = 0. \quad (10.18)$$

We easily deduce

$$\frac{\partial h}{\partial t} + \frac{\partial h \bar{u}}{\partial x} = 0, \quad (10.19)$$

where we have introduced depth-averaged values defined as

$$\bar{f}(x, t) = \frac{1}{h(x, t)} \int_0^{h(x, t)} f(x, y, t) dy. \quad (10.20)$$

The same procedure is applied to the momentum balance equation: $\rho d\mathbf{u}/dt = \rho \mathbf{g} + \nabla \cdot \boldsymbol{\sigma}$, where $\boldsymbol{\sigma}$ denotes the stress tensor. Without difficulty, we can deduce the averaged momentum equation from the x -component of the momentum equation:

$$\rho \left(\frac{\partial h\bar{u}}{\partial t} + \frac{\partial h\bar{u}^2}{\partial x} \right) = \rho gh \sin \theta + \frac{\partial h\bar{\sigma}_{xx}}{\partial x} - \tau_b, \quad (10.21)$$

where we have introduced the bottom shear stress: $\tau_b = \sigma_{xy}(x, 0, t)$. In the present form, the motion equation system (10.19)–(10.21) is not closed since the number of variables exceeds the number of equations. A common approximation involves introducing a parameter (sometimes called the Boussinesq momentum coefficient), which links the mean velocity to the mean square velocity.

$$\bar{u}^2 = \frac{1}{h} \int_0^h u^2(y) dy = \alpha \bar{u}^2. \quad (10.22)$$

Usually α is set to unity, but this may cause trouble when computing the head structure (Hogg and Pritchard 2004; Ancey et al. 2006; 2007). A point often neglected is that the shallow-flow approximation is in principle valid for flow regimes that are not too far away from a steady uniform regime. In flow parts where there are significant variations in the flow depth (e.g., at the leading edge and when the flow widens or narrows substantially), corrections should be made to the first-order approximation of stress. Recent studies, however, showed that errors made with the shallow-flow approximation for the leading edge are not significant (Ancey et al. 2007; Ancey and Cochard 2009; Ancey et al. 2009).

A considerable body of work has been published on this method for Newtonian and non-Newtonian fluids, including viscoplastic (Coussot 1997; Huang and García 1998; Siviglia and Cantelli 2005), power-law (Fernández-Nieto et al. 2010), and granular materials (Savage and Hutter 1989; Gray et al. 1998; Pouliquen and Forterre 2002; Iverson and Denlinger 2001; Bouchut et al. 2003; Chugunov et al. 2003; Pudasaini and Hutter 2003; Kerswell 2005). In this chapter, we will provide two applications for dense flows in Section 10.5.2: viscoplastic and friction Coulomb materials. Extension to dilute flows is outlined in Section 10.6.2. In Section 10.7.2, we will also show how the depth-averaged equations can be used to delineate the flow regimes and infer their main features.

10.4.6 Asymptotic Expansions

On many occasions, flows are not in equilibrium, but deviate slightly from it. In this context, it is often convenient to use asymptotic expansions for the velocity field (Holmes 1995):

$$u(x, y, t) = u_0(x, y, t) + \epsilon u_1(x, y, t) + \epsilon^2 u_2(x, y, t) + \dots,$$

where ϵ is a small number (e.g., the aspect ratio $\epsilon = H_*/L_*$ in equations (10.6)–(10.7)) and $u_i(x, y, t)$ are functions to be determined; usually, u_0 is the velocity field when the flow is at equilibrium and u_i represents perturbations to this equilibrium state. Substituting u by this expansion into the local governing equations such as equations (10.6)–(10.7) leads to a hierarchy of equations of increasing order. Most of the time, only the zero-order solution and the first-order correction are computed. Examples will be provided with the computation of an elongating viscoplastic flow in Section 10.5.3.

10.5 Dense Flows

We address the issue of dense flows, for which the effect of the surrounding air is neglected. We first illustrate the sliding block approach by outlining the Voellmy-Salm-Gubler model, which is one of the most popular models worldwide for computing the main features of extreme snow avalanches (Salm et al. 1990). In Section 10.5.2, we see two applications of the flow-depth averaged equations (frictional and viscoplastic fluids). We end this section with the use of asymptotic expansions to describe the motion of viscoplastic flows (see Section 10.5.3).

10.5.1 Simple Models

The avalanche is assumed to behave as a rigid body that moves along an inclined plane. The position of the center of mass is given by its abscissa x in the downward direction. The momentum equation is

$$\frac{du}{dt} = g \sin \theta - \frac{F}{m}, \quad (10.23)$$

with m the avalanche mass, u its velocity, θ the mean slope of the path, and F the frictional force. In this model, the sliding block is subject to a frictional force combining a solid-friction component and a square-velocity component:

$$F = mg \frac{u^2}{\xi h} + \mu mg \cos \theta, \quad (10.24)$$

with h the mean flow depth of the avalanche, μ a friction coefficient related to the snow fluidity, and ξ a coefficient of dynamic friction related to path roughness. If these last two parameters cannot be measured directly, they can be adjusted from several series of past events. It is generally accepted that the friction coefficient μ depends only on the avalanche size and ranges from 0.4 (small avalanches) to 0.155 (very large avalanches) (Salm et al. 1990); in practice, lower values can be observed for large-volume avalanches (Ancey et al. 2004). Likewise, the dynamic parameter ξ reflects the influence of the path on avalanche motion. When an avalanche runs

down a wide-open rough slope, ξ is close to $1,000 \text{ m s}^{-2}$. Conversely, for avalanches moving down confined straight gullies, ξ can be taken as being equal to 400 m s^{-2} . In a steady state, the velocity is directly inferred from the momentum balance equation

$$u = \sqrt{\xi h \cos \theta (\tan \theta - \mu)}. \quad (10.25)$$

According to this equation, two flow regimes can occur depending on path inclination. For $\tan \theta > \mu$, (10.25) has a real solution and a steady regime can occur. For $\tan \theta < \mu$, there is no real solution; the frictional force (10.24) outweighs the downward component of the gravitational force. It is therefore considered that the flow slows. The point of the path for which $\tan \theta = \mu$ is called the characteristic point (point P). It plays an important role in avalanche dynamics since it separates flowing and runout phases. In the stopping area, we deduce from the momentum equation that the velocity decreases as follows:

$$\frac{1}{2} \frac{du^2}{dx} + u^2 \frac{g}{\xi h} = g \cos \theta (\tan \theta - \mu). \quad (10.26)$$

The runout distance is easily inferred from (10.26) by assuming that at a point $x = 0$, the avalanche velocity is u_p . In practice the origin point is point P but attention must be paid to the fact that, according to (10.25), the velocity at point P should be vanishing; a specific procedure has been developed to avoid this shortcoming (Salm et al. 1990). Neglecting the slope variations in the stopping zone, we find that the runout distance x_s (point of farthest reach) counted from point P is

$$x_s = \frac{\xi h}{2g} \ln \left(1 + \frac{u_p^2}{\xi h \cos \theta (\mu - \tan \theta)} \right). \quad (10.27)$$

This model enables us to easily compute the runout distance, the maximum velocities reached by the avalanche on various segments of the path, the flow depth (by assuming that the mass flow rate is constant and given by the initial flow rate just after the release), and the impact pressure.

10.5.2 Depth-Averaged Equations

The Saint-Venant equations consist of the following depth-averaged mass and momentum balance equations

$$\frac{\partial h}{\partial t} + \frac{\partial h \bar{u}}{\partial x} = 0, \quad (10.28)$$

$$\rho \left(\frac{\partial h \bar{u}}{\partial t} + \frac{\partial h \bar{u}^2}{\partial x} \right) = \rho g h \sin \theta - \frac{\partial h \bar{p}}{\partial x} + \frac{\partial h \bar{\sigma}_{xx}}{\partial x} - \tau_b, \quad (10.29)$$

where we have introduced the bottom shear stress $\tau_b = \sigma_{xy}(x, 0, t)$ and we assume $\overline{u^2} = \bar{u}^2$; the flow-depth averaged pressure is found to be lithostatic

$$\bar{p} = \frac{1}{2} \rho g h \cos \theta.$$

Within the framework of the long-wave approximation, we assume that longitudinal motion outweighs vertical motion; for any quantity m related to motion, we have $\partial m / \partial y \gg \partial m / \partial x$. This allows us to consider that every vertical slice of flow can be treated as if it were locally uniform. In such conditions, it is possible to infer the bottom shear stress by extrapolating its steady-state value and expressing it as a function of \bar{u} and h . For instance, for viscoplastic fluids, a common constitutive equation is the Herschel-Bulkley law (10.8). By relating the bottom shear rate to the flow-depth averaged velocity, Coussot (1997) showed that the bottom shear stress is a solution to the implicit equation

$$\frac{\bar{u}}{h} = \frac{n}{2n+1} \left(\frac{\tau_b}{K} \right)^{1/n} \left(1 - \frac{\tau_c}{\tau_b} \right)^{1+1/n} \left(1 + \frac{n}{n+1} \frac{\tau_c}{\tau_b} \right),$$

for Herschel-Bulkley fluids, with n , K , and τ_c the constitutive parameters introduced in equation (10.8). Note that this equation admits physical solutions provided that $\tau_b > \tau_c$. For $\tau_b \leq \tau_c$, the material comes to a halt. For $n = 1/3$, Coussot (1997) provided the following approximation (accurate to within 5%),

$$\tau_b = \tau_c \left(1 + a \left(\frac{\tau_c}{K} \right)^{-9/10} \left(\frac{\bar{u}}{h} \right)^{3/10} \right),$$

with $a = 1.93$ for an infinitely wide plane and $a = 1.98$ for a semi-cylindrical flume.

For Coulomb materials, the same procedure can be repeated. The only modification concerns the momentum balance equation (10.29), which takes the form (Savage and Hutter, 1989; Iverson and Denlinger, 2001):

$$\rho \left(\frac{\partial h \bar{u}}{\partial t} + \frac{\partial h \bar{u}^2}{\partial x} \right) = \rho g h \left(\sin \theta - k \cos \theta \frac{\partial h}{\partial x} \right) - \tau_b, \quad (10.30)$$

with k a proportionality coefficient between the normal stresses $\bar{\sigma}_{xx}$ and $\bar{\sigma}_{yy}$, which is computed by assuming a limited Coulomb equilibrium in compression ($\partial_x \bar{u} < 0$) or extension ($\partial_x \bar{u} > 0$); the coefficient is called the *active/passive pressure* coefficient. In equation (10.30), the bottom shear stress can be computed by using the Coulomb law $\tau_b = (\bar{\sigma}_{yy}|_{y=0} - p_b) \tan \varphi$, with $\bar{\sigma}_{yy}|_{y=0} = \bar{\rho} g h \cos \theta$ and p_b the pore pressure at the bed level.

Analytical solutions can be obtained for the Saint-Venant equations. Most of them were derived by seeking self-similarity solutions; see (Savage and Nohguchi 1988; Savage and Hutter 1989; Chugunov et al. 2003) for the Coulomb model and (Hogg and Pritchard, 2004) for viscoplastic and hydraulic models. Some solutions can also be

obtained using the method of characteristics. We will present two applications based on these methods.

In the first application, we use the fact that the Saint-Venant equations for Coulomb materials are structurally similar to those used in hydraulics when the bottom drag can be neglected. The only difference lies in the nonhydrostatic pressure term and the source term (bottom shear stress). However, using a change in variable makes it possible to retrieve the usual shallow-water equations and seek similarity solutions to derive the Ritter solutions (Mangeney et al. 2000; Karelsky et al. 2000; Kerswell 2005). The Ritter solutions are the solutions to the so-called dam-break problem, where an infinite volume of material at rest is suddenly released and spreads over a dry bed (i.e., no material lying along the bed). Much attention has been paid to this problem, notably in geophysics, because it is used as a paradigm for studying rapid surge motion. We pose

$$x^* = x - \frac{\delta}{2}t^2, \quad t^* = t, \quad u^* = u - \delta t, \quad \text{and} \quad h^* = h,$$

where we introduced the parameter $\delta = g \cos \theta (\tan \theta - \mu)$. We deduce

$$\frac{\partial h^*}{\partial t^*} + \frac{\partial h^* u^*}{\partial x^*} = 0, \quad (10.31)$$

$$\frac{\partial u^*}{\partial t^*} + u^* \frac{\partial u^*}{\partial x^*} + gk \cos \theta \frac{\partial h^*}{\partial x^*} = 0. \quad (10.32)$$

For the dam-break problem, the initial and boundary conditions are

$$\begin{aligned} -\infty < x < \infty, \quad u(x, 0) &= 0, \\ x < 0, \quad h(x, 0) &= h_i, \\ x > 0, \quad h(x, 0) &= 0. \end{aligned} \quad (10.33)$$

The analytical solutions to equations (10.31)–(10.32) are the well-known Ritter solutions. We are looking for a similarity solution in the form (Gratton and Vigo 1994)

$$\bar{u}^* = t^{*\beta/\alpha} U(\zeta^*) \quad \text{and} \quad h^* = t^{*\gamma/\alpha} H(\zeta^*),$$

with $\zeta^* = x^*/t^{*\alpha}$ the similarity variable, and H and U two unknown functions. Substituting \bar{u}^* and h^* with their similarity forms into (10.31)–(10.32), we find: $\beta + \alpha = 1$ and $\gamma + 2\alpha = 2$. For this solution to satisfy the initial and boundary conditions, we must pose $\beta = \gamma = 0$; hence, $\alpha = 1$. We then infer

$$\begin{pmatrix} H & U - \zeta^* \\ U - \zeta^* & kg \cos \theta \end{pmatrix} \cdot \begin{pmatrix} U' \\ H' \end{pmatrix} = 0,$$

where the prime denotes the ζ^* -derivative. For this system to admit a nonconstant solution, its determinant must vanish, which leads to $kgH \cos \theta = (U - \zeta^*)^2$. On

substituting this relation into the preceding system, we deduce $U' = 2\zeta^*/3$, thus, $U = 2(\zeta^* + c)/3$, where c is a constant of integration, $H = 4(c - \frac{1}{2}\zeta^*)^2/(9kg \cos\theta)$. The constant c is found using the boundary conditions and by assuming that the undisturbed flow slides at constant velocity δt : $c = \sqrt{kg h_i \cos\theta}$. Returning to the original variables, we find

$$\bar{u}(x, t) = \bar{u}^* + \delta t = \frac{2}{3} \left(\frac{x}{t} + \delta t + c \right), \quad (10.34)$$

$$h(x, t) = \frac{1}{9kg \cos\theta} \left(-\frac{x}{t} + \frac{\delta}{2}t + 2c \right)^2. \quad (10.35)$$

The boundary conditions also imply that the solution is valid over the ζ -range $[-c - \delta t, 2c + \delta t/2]$; the lower bound corresponds to the upstream condition $\bar{u} = 0$, while the upper bound is given by the downstream condition $h = 0$. It is worth noting that the front velocity $u_f = 2c + \delta t/2$ is constantly increasing or decreasing depending on the sign of δ . When $\delta < 0$ (friction in excess of slope angle), the front velocity vanishes at $t = 4c/|\delta|$. Figure 10.14 shows that the shape of the tip region is parabolic at short times ($\delta t \ll c$), in agreement with experimental data (Balmforth and Kerswell 2005; Siavoshi and Kudrolli 2005). Solutions corresponding to finite released volumes were also obtained by Ancey et al. (2008), Hogg (2006), and Savage and Nohguchi (1988); and Savage and Hutter (1989).

In the second application, we use the method of characteristics to find a solution to the governing equations for Bingham flows that are stretched thin layers when they are nearly steady uniform. In a steady uniform regime, the velocity field can be obtained by using the Bingham law (10.8) and equating it to the shear stress distribution:

$$\tau = \rho g(h - y) \sin\theta = \tau_c + K \frac{du}{dy}.$$

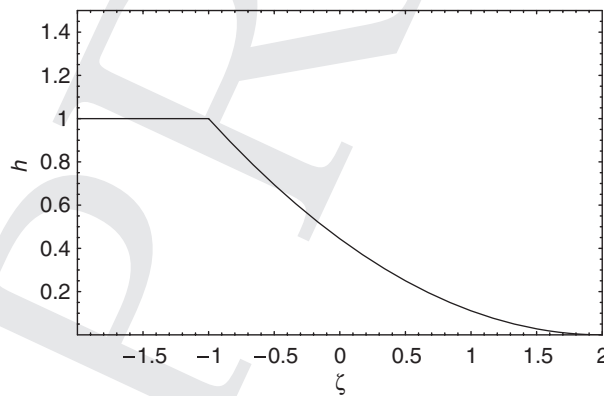


Figure 10.14. Flow-depth profile generated just after the wall retaining a granular material is removed. Computations made with $c = 1$ m/s. The similarity variable ζ is $\zeta = x/t$.

On integrating twice, we obtain the depth-averaged velocity

$$\bar{u}_s = u_p \left(1 - \frac{h_0}{3h} \right), \quad (10.36)$$

where u_p is the plug velocity

$$u_p = \frac{\rho g h_0^2 \sin \theta}{2K},$$

with h the flow depth and $h_0 = h - \tau_c / (\rho g \sin \theta)$ the yield-surface elevation; h_0 must be positive, or no steady flow occurs. For mild slopes, when the aspect ratio ϵ is very low, the inertial and pressure contributions can be neglected (see dimensional analysis in Section 10.4.1). This means that the depth-averaged velocity is very close to the mean velocity (10.36) reached for steady uniform flows. We then use the kinematic-wave approximation introduced by Lighthill and Whitham (1955) to study floods on long rivers; this approximation has been then extensively used in hydraulic applications (Hunt 1994; Huang and Garcia 1997, 1998). It involves substituting the steady-state value \bar{u}_s for the mean velocity into the mass balance equation (10.28)

$$\frac{\partial h}{\partial t} + \frac{\partial}{\partial x} u_p \left(h - \frac{h_0}{3} \right) = 0. \quad (10.37)$$

Introducing the plug thickness $h_p = h - h_0 = \tau_c / (\rho g \sin \theta)$, we obtain an expression that is a function of h and its time and space derivative

$$\frac{\partial h}{\partial t} + G \left(h^2 - h h_p \right) \frac{\partial h}{\partial x} = 0,$$

with $G = \rho g \sin \theta / K$. The governing equation takes the form of a nonlinear advection equation, which can be solved using the method of characteristics (LeVeque 2002).

Using the chain rule for interpreting this partial differential equation (10.37), we can show that it is equivalent to the following ordinary equation

$$\frac{dh}{dt} = 0, \quad (10.38)$$

along the characteristic curve

$$\frac{dx}{dt} = \lambda(h), \quad (10.39)$$

in the (x, t) plane, with $\lambda(h) = Gh(h - h_p)$. Equation (10.38) shows that the flow depth is constant along the characteristic curve; hence, the characteristic curves are straight lines, the slope of which are given by the right-hand side term $\lambda(h)$ in equation (10.39). These characteristic curves can be used to solve an initial value problem, where the initial value of h is known over a given interval: $h = h_i(x_i)$ (at

$t = 0$). The value of h along each characteristic curve is the value of h at the initial point $x(0) = x_i$. We can thus write

$$h(x, t) = h_i(x_i) = h_i(x - \lambda(h_i(x_i))t).$$

It is worth noting that because of the nonlinearity of equation (10.37), a smooth initial condition can generate a discontinuous solution (shock) if the characteristic curves intersect, since at the point of intersection h takes (at least) two values (LeVeque 2002).

10.5.3 Elongating Viscoplastic Flows

Slow motion of a viscoplastic material has been investigated by Liu and Mei (1990a; 1990b), Mei et al. (2001), Coussot et al. (1996), Balmforth and Craster (1999); Balmforth et al. (2002), Matson and Hogg (2007), Ancey and Cochard (2009), and Hogg and Matson (2009).

Here we consider that the shear stress is given by (10.8) with $n = 1$. Taking the two dominant contributions in equations (10.6)–(10.7), integrating, and returning to the physical variables, we deduce

$$\tau = \sigma_{xy} = \rho g \cos \theta (h - y) \left(\tan \theta - \frac{\partial h}{\partial x} \right), \quad (10.40)$$

$$p = \rho g (h - y) \cos \theta. \quad (10.41)$$

The bottom shear stress is then found to be $\tau_b = \sigma_{xy}|_{y=0}$. For bottom shear stresses in excess of the yield stress τ_c , flow is possible. When this condition is satisfied, there is a yield surface at depth $y = h_0$ within the bulk, along which the shear stress matches the yield stress

$$\tau|_{y=h_0} = \rho g \cos \theta (h - h_0) \left(\tan \theta - \frac{\partial h}{\partial x} \right) = \tau_c. \quad (10.42)$$

The yield surface separates the flow into two layers (Liu and Mei 1990a; Balmforth and Craster 1999): the bottom layer, which is sheared, and the upper layer or plug layer, where the shear rate is nearly zero. Indeed, using an asymptotic analysis, Balmforth and Craster (1999) demonstrated that in the so-called plug layer, the shear rate is close to zero, but nonzero. This result may seem anecdotal, but it is in fact of great importance since it resolves a number of paradoxes raised about viscoplastic solutions (these paradoxes refer to the existence or nonexistence of true unyielded plug regions as described, for instance, by Piau (1996)).

On integrating the shear-stress distribution, we can derive a governing equation for the flow depth $h(x, t)$. For this purpose, we must specify the constitutive equation. For the sake of simplicity, we consider a Bingham fluid in one-dimensional flows as

Liu and Mei (1990a) did; the extension to Herschel-Bulkley and/or two-dimensional flows can be found in (Balmforth and Craster, 1999; Balmforth et al., 2002; Mei and Yuhi, 2001; Ancey and Cochard, 2009). In the sheared zone, the velocity profile is parabolic

$$u(y) = \frac{\rho g \cos \theta}{K} \left(\tan \theta - \frac{\partial h}{\partial x} \right) \left(h_0 y - \frac{1}{2} y^2 \right) \text{ for } y \leq h_0,$$

while the velocity is constant to leading order within the plug

$$u(y) = u_0 = \frac{\rho g h_0^2 \cos \theta}{K} \left(\tan \theta - \frac{\partial h}{\partial x} \right) \text{ for } y \geq h_0,$$

The flow rate is then

$$q = \int_0^h u(y) dy = \frac{\rho g h_0^2 (3h - h_0) \cos \theta}{6K} \left(\tan \theta - \frac{\partial h}{\partial x} \right). \quad (10.43)$$

Integrating the mass balance equation over the flow depth provides

$$\frac{\partial h}{\partial t} + \frac{\partial q}{\partial x} = 0. \quad (10.44)$$

Substituting q with its expression (10.43) and the yield surface elevation h_0 with equation (10.42) into equation (10.44), we obtain a governing equation for h , which takes the form of a nonlinear advection diffusion equation

$$\frac{\partial h}{\partial t} = \frac{\partial}{\partial x} \left[F(h, h_0) \left(\frac{\partial h}{\partial x} - \tan \theta \right) \right], \quad (10.45)$$

with $F = \rho g h_0^2 (3h - h_0) \cos \theta / (6K)$.

A typical application of this analysis is the derivation of the shape of a viscoplastic deposit. Contrary to a Newtonian fluid, the flow depth of a viscoplastic fluid cannot decrease indefinitely when the fluid spreads out along an infinite plane. Because of the finite yield stress, when it comes to rest, the fluid exhibits a nonuniform flow-depth profile, where the pressure gradient is exactly balanced by the yield stress. On an infinite horizontal plane, the bottom shear stress must equal the yield stress. Using equation (10.40) with $\theta = 0$ and $y = 0$, we eventually obtain (Liu and Mei 1990a)

$$\sigma_{xy}|_{y=0} = \tau_c = -\rho g h \frac{\partial h}{\partial x}, \quad (10.46)$$

which, on integrating, provides

$$h(x) - h_i = \sqrt{\frac{2\tau_c}{\rho g} (x_i - x)}, \quad (10.47)$$

where $h = h_i$ at $x = x_i$ is a boundary condition. This equation shows that the deposit-thickness profile depends on the square root of the distance. This is good agreement



Figure 10.15. Lobes of a debris-flow deposit near the Rif Paulin stream (Hautes-Alpes, France).

with field observations (Coussot et al. 1996); Figure 10.15 shows the lobe of a debris-flow deposit whose profile can be closely approximated by (10.47).

When the slope is nonzero, an implicit solution for $h(x)$ to equation (10.40) is found (Liu and Mei, 1990a)

$$\tan\theta(h(x) - h_i) + \frac{\tau_c}{\rho g \cos\theta} \log \left[\frac{\tau_c - \rho g h \sin\theta}{\tau_c - \rho g h_i \sin\theta} \right] = \tan^2\theta(x - x_i). \quad (10.48)$$

The shape of a static two-dimensional pile of viscoplastic fluid was investigated by Coussot et al. (1996), Mei and Yuhi (2001), Osmond and Griffiths (2001), and Balmforth et al. (2002). Balmforth et al. (2002) derived an exact solution, whereas Coussot et al. (1996) used numerical methods or ad hoc approximations to solve the two-dimensional equivalent to equation (10.40). Similarity solutions to equation (10.45) have also been provided by Balmforth et al. (2002) in the case of a viscoplastic flow down a gently inclined, unconfined surface with a time-varying source at the inlet. Ancy and Cocharde (2009) used matched-asymptotic expansions to build approximate analytical solutions for the movement of a finite volume of Herschel-Bulkley fluid down a flume. Matson and Hogg (2007) and Hogg and Matson (2009) investigated the slumping motion of a fixed volume on a plane and down an inclined slope.

10.6 Dilute Inertia-Dominated Flows

10.6.1 Sliding Block Model

The first-generation models of airborne avalanches used the analogy of density currents along inclined surfaces. Extending a model proposed by Ellison and Turner (1959) on the motion of an inclined plume, Hopfinger and Tochon-Danguy (1977) inferred the mean velocity of a steady current, assumed to represent the avalanche body behind the head. They found that the front velocity of the current was fairly independent of the bed slope. The second generation of models has considered the avalanche as a finite-volume, turbulent flow of a snow suspension. Kulikovskiy and Svehnikova (1977) set forth a fairly simple theoretical model (the KS model) in which the cloud was assimilated to a semi-elliptic body whose volume varied with time. The kinematics were entirely described by the mass center position and two geometric parameters of the cloud (the two semi-axes of the ellipsis). The cloud density can vary depending on air and snow entrainments. Kulikovskiy and Svehnikova obtained a set of four equations describing the mass, volume, momentum, and Lagrangian kinetic energy balances. The idea was subsequently redeveloped by many authors, including Beghin et al. (1981), Beghin and Brugnot (1983), Fukushima and Parker (1990), Beghin and Olagne (1991), Fukushima et al. (2000), Ancey (2004), and Turnbull et al. (2007).

Here we outline the KSB model as presented and extended by Ancey (2004). We will consider the two-dimensional motion of a cloud along a plane inclined at an angle θ with respect to the horizontal. Figure 10.16 depicts a typical cloud entraining particles from the bed. In the following, H denotes the cloud height, L its length, m its mass, and V its volume. The cloud velocity is $U = dx/dt$, but since the body is deformable, the velocity varies inside the body. The front position is given by the abscissa x_f and its velocity is $U_f = dx_f/dt$. The volume solid concentration is ϕ ; it is assumed that the cloud is a homogeneous suspension of particles of density ρ_p (no density stratification) in the ambient fluid of density ρ_a and viscosity μ_a . The bulk cloud density is then $\bar{\rho} = \phi\rho_p + (1 - \phi)\rho_a$. Ahead of the front, there is a particle bed made up of the same particles as the cloud and whose thickness is denoted by h_n . The apparent density of the layer is $\rho_s = \phi_m\rho_p + (1 - \phi_m)\rho_a$, where ϕ_m denotes the maximum random volume concentration of particles.

The surface area (per unit width) exposed to the surrounding fluid is denoted by S and can be related to H and L as follows: $S = k_s\sqrt{HL}$, where k_s is a shape factor. Here we assume that the cloud keeps a semielliptic form whose aspect ratio $k = H/L$ remains constant during the cloud run when the slope is constant. We then obtain

$$k_s = E(1 - 4k^2)/\sqrt{k}, \quad (10.49)$$

where E denotes the elliptic integral function. Similarly, we can express the volume V (per unit width) as $V = k_vHL$, where k_v is another shape factor for a half ellipsis.

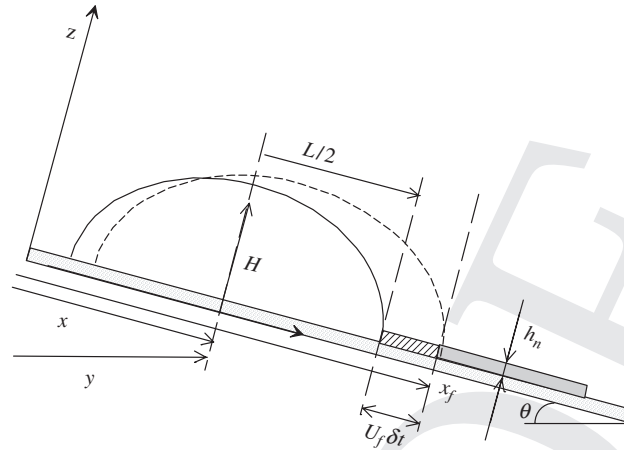


Figure 10.16. Sketch of the physical system studied here: The powder-snow avalanche is assumed to be a half ellipse whose volume grows with time. The major axis is the length $L(t)$, the semiminor axis is the flow depth $H(t)$. Since the body is deformable, the velocity varies with position: $U(t)$ refers to the velocity of the center of mass, while $U_f(t)$ is the velocity at the front $x = x_f(t)$. In the course of motion, the avalanche entrains snow from the snow cover; the thickness of the entrained snow layer is h_n .

Here we have

$$k_v = \pi/4. \quad (10.50)$$

In the following, we will also need to use the volume, height, and length growth rates

$$\alpha_v = \frac{1}{\sqrt{V}} \frac{dV}{dx}, \quad \alpha_h = \frac{dH}{dx}, \quad \alpha_l = \frac{dL}{dx}. \quad (10.51)$$

Experimentally, it is easier to measure the growth rates by deriving the quantity at hand by the front abscissa instead of by the mass center abscissa; we will refer to these rates as

$$\tilde{\alpha}_v = \frac{1}{\sqrt{V}} \frac{dV}{dx_f}, \quad \tilde{\alpha}_h = \frac{dH}{dx_f}, \quad \tilde{\alpha}_l = \frac{dL}{dx_f}. \quad (10.52)$$

Note that all these quantities are interrelated. For instance, using $x = x_f - L/2$, we find: $\tilde{\alpha}_h = (dH/dx)(dx/dx_f) = \alpha_h(1 - \tilde{\alpha}_l/2)$. Similarly, using the definition of k and k_v , we obtain

$$\alpha_h = \frac{\alpha_v}{2} \sqrt{\frac{k}{k_v}} \quad \text{and} \quad \alpha_l = \frac{\alpha_v}{2\sqrt{k k_v}}. \quad (10.53)$$

The KSB model outlined here includes three equations: volume, mass, and momentum balances. The volume variations mainly result from the entrainment of the ambient, less-dense fluid. To express the volume balance equation, the most common

assumption is to state that the volume variations come from the entrainment of the ambient fluid into the cloud and that the inflow rate is proportional to the exposed surface area and a characteristic velocity u_e . This leads to the equation

$$\frac{dV}{dt} = E_v S u_e, \quad (10.54)$$

where E_v is the bulk entrainment coefficient and is a function of the Richardson number (10.1). According to the flow conditions, different expressions of E_v have been drawn from experiments. Interestingly enough, the value of E_v has been expressed very differently depending on whether the current is steady or unsteady. There is, however, no clear physical reason that justifies this partitioning. Indeed, for most experiments, the currents were gradually accelerating, and mixing still occurred as a result of the development of Kelvin-Helmholtz billows, thus very similarly to the steady case. This observation prompted Ancy (2004) to propose a new expression of the entrainment coefficient for clouds, which holds for both steady and slightly unsteady conditions: Ancy (2004) related E_v (or α_v) as a function of Ri (instead of θ as done by previous authors): for $Ri \leq 1$, $\alpha_v = e^{-1.6Ri^2}$, while for $Ri > 1$, $\alpha_v = 0.2/Ri$.

The cloud mass can vary as a result of the entrainment of the surrounding fluid and/or the entrainment of particles from the bed. The former process is easily accounted for. During a short time increment δt , the cloud volume V is increased by a quantity δV mainly as a result of the air entrainment, thus the corresponding increase in the cloud mass is $\rho_a \delta V$. The latter process is less well known. Using an analogy with sediment erosion in rivers and turbidity currents, Fukushima and Parker (1990) assumed that particles are continuously entrained from the bed when the drag force exerted by the cloud on the bed exceeds a critical value. This implies that the particle entrainment rate is controlled by the surface of the bed in contact with the cloud and the mismatch between the drag force and the threshold of motion. Here, since in extreme conditions the upper layers of the snowcover made up of new snow of weak cohesion can be easily entrained, all the recent layer ahead of the cloud may be incorporated into the cloud. When the front has traveled a distance $U_f \delta t$, where U_f is the front velocity, the top layer of depth h_n and density ρ_s is entirely entrained into the cloud (see Figure 10.16). The resulting mass variation (per unit width) is written: $\rho_s U_f h_n \delta t$. At the same time, particles settle with a velocity v_s . During the time step δt , all the particles contained in the volume $L v_s \delta t$ deposit. Finally, by taking the limit $\delta t \rightarrow 0$, we can express the mass balance equation as follows:

$$\frac{dm}{dt} = \rho_a \frac{dV}{dt} + \rho_s U_f h_n - \phi \rho_s L v_s,$$

where $m = \bar{\rho} V$ is the cloud mass. Usually the settling velocity v_s is very low compared to the mean forward velocity of the front so that it is possible to ignore the third term on the right-hand side of the preceding equation. We then obtain the following simplified

equation:

$$\frac{d\Delta\bar{\rho}V}{dt} = \rho_s U_f h_n. \quad (10.55)$$

The cloud undergoes the driving action of gravity and the resisting forces due to the ambient fluid and the bottom drag. The driving force per unit volume is $\bar{\rho}g \sin \theta$. Most of the time, the bottom drag effect plays a minor role in the accelerating and steady-flow phases but becomes significant in the decelerating phase (Hogg and Woods 2001). Since we have set aside a number of additional effects (particle sedimentation, turbulent kinetic energy), it seems reasonable to also discard this frictional force. The action of the ambient fluid can be broken into two terms: a term analogous to a static pressure (Archimedes' theorem), equal to $\rho_a V g$, and a dynamic pressure. As a first approximation, the latter term can be evaluated by considering the ambient fluid as an inviscid fluid in an irrotational flow. On the basis of this approximation, it can be shown that the force exerted by the surrounding fluid on the half cylinder is $\rho_a V \chi dU/dt$, where

$$\chi = k \quad (10.56)$$

is called the *added mass coefficient*. Since at the same time volume V varies and the relative motion of the half cylinder is parallel to its axis of symmetry, we finally take $\rho_a \chi d(UV)/dt$. Note that this parameter could be ignored for light interstitial fluids (e.g., air), whereas it has a significant influence for heavy interstitial fluids (basically, water). Thus, the momentum balance equation can be written as

$$\frac{d(\bar{\rho} + \chi\rho_a)VU}{dt} = \Delta\bar{\rho}gV \sin \theta. \quad (10.57)$$

Analytical solutions can be found in the case of a Boussinesq flow ($\bar{\rho}/\rho_a \rightarrow 1$); for the other cases, numerical methods must be used. In the Boussinesq limit, since the final analytical solution is complicated, we provide only an asymptotic expression at early and late times. To simplify the analytical expressions without loss of generality, we take: $U_0 = 0$ and $x_0 = 0$ and assume that the erodible snowcover thickness h_n and density ρ_s are constant. The other initial conditions are at $t = 0$ and $x = 0$, $H = H_0$, $L = L_0$, $V_0 = k_v H_0 L_0$, and $\bar{\rho} = \bar{\rho}_0$. At short times, the velocity is independent of the entrainment parameters and the initial conditions ($\bar{\rho}_0$ and V_0):

$$U \propto \sqrt{2gx \sin \theta \frac{\Delta\rho_0}{\Delta\rho_0 + (1 + \chi)\rho_a}} \approx \sqrt{2gx \sin \theta}, \quad (10.58)$$

where we used $\rho_a \ll \Delta\bar{\rho}_0$. This implies that the cloud accelerates vigorously in the first instants ($dU/dx \rightarrow \infty$ at $x=0$), and then its velocity grows more slowly. At long times for an infinite plane, the velocity reaches a constant asymptotic velocity that

depends mainly on the entrainment conditions for flows in the air

$$U_\infty \propto \sqrt{\frac{2gh_n(1 + \frac{\alpha_l}{2}) \sin \theta \varrho_s}{\alpha_v^2(1 + \chi)\varrho_a}}. \quad (10.59)$$

Because of the slow growth of the velocity, this asymptotic velocity is reached only at very long times. Without particle entrainment, the velocity reaches a maximum at approximately $x_m^2 = (2\varrho_0/3\varrho_a)\alpha_v^{-2}V_0/(1 + \chi)$:

$$U_m^2 \approx \frac{4}{\sqrt{3}} \sqrt{\frac{\varrho_0}{\varrho_a}} \frac{g\sqrt{V_0} \sin \theta}{\alpha_v \sqrt{1 + \chi}},$$

then it decreases asymptotically as

$$U \propto \sqrt{\frac{8\Delta\varrho_0}{3\varrho_a} \frac{gV_0 \sin \theta}{x} \frac{1}{\alpha_v^2(1 + \chi)}}. \quad (10.60)$$

In this case, the front position varies with time as

$$x_f \propto (g'_0 V_0 \sin \theta)^{1/3} t^{2/3} \quad (10.61)$$

These simple calculations show the substantial influence of the particle entrainment on cloud dynamics. In the absence of particle entrainment from the bed, the fluid entrainment has a key role since it directly affects the value of the maximum velocity that a cloud can reach.

Here, we examine only the avalanche of 25 February 1999, for which the front velocity was recorded. In Figure 10.17, we have reported the variation in the mean front velocity U_f as a function of the horizontal downstream distance y_f . The dots correspond to the measured data, and the curves represent the solution obtained by integrating equations (10.54)–(10.57) numerically and by assuming that the growth rate coefficient depends on the overall Richardson number (solid line). For the initial conditions, we assume that $u_0 = 0$, $h_0 = 2.1$ m, $l_0 = 20$ m, and $\varrho_0 = \varrho_s = 150$ kg/m³. Because of the steep slope between the origin and the elevation $z = 1,800$ m ($y = 1,250$ m) we have considered that, on average, the released snow layer h_n is 0.7 m thick and is entirely entrained into the avalanche. Using $\alpha_v \propto Ri^{-1}$ for $Ri \gg 1$, we apply the following relationship: for $Ri \leq 1$, $\alpha_v = e^{-1.6Ri^2}$, whereas for $Ri > 1$, we take $\alpha_v = 0.2/Ri$.

As shown in Figure 10.17, the avalanche accelerated vigorously after the release and reached velocities as high as 80 m/s. The velocity variation in the release phase is fairly well described by the KSB model. The model predicts a bell-shaped velocity variation, whereas field data provide a flatter velocity variation. The computed flow depth at $z = 1,640$ m is approximately 60 m, which is consistent with the value estimated from the videotapes. To evaluate the sensitivity of the simulation results, we examined different values of the erodible mass. In Figure 10.17, we have reported the comparison between

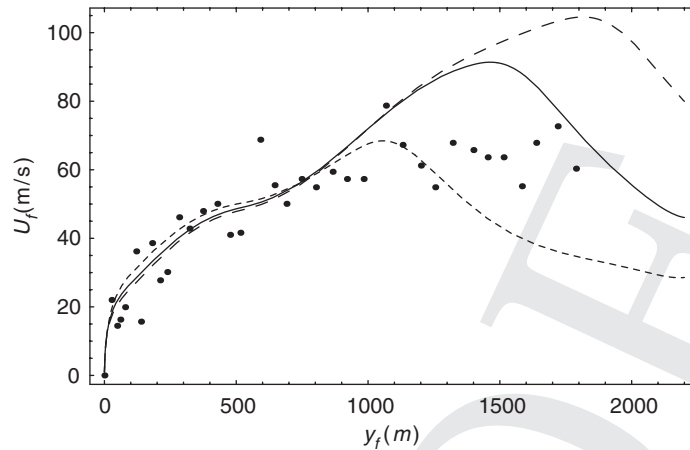


Figure 10.17. Dependence of the front velocity on the erodible mass. Solid line, $\rho_s h_n = 105 \text{ kg/m}^2$; dashed line, $\rho_s h_n = 50 \text{ kg/m}^2$; long-dashed line, $\rho_s h_n = 150 \text{ kg/m}^2$. After Ancey (2004).

field data and computations made with three different assumptions: $\rho_s h_n = 50, 105$, or 150 kg/m^2 . It can be seen that there is no significant variation in the computed velocities in the accelerating phase, but both the maximum velocity and the position at which the maximum velocity is reached depend on the $\rho_s h_n$ value. By increasing the erodible mass per unit surface from 50 to 150 kg/m^2 , the maximum velocity is increased from 69 m/s to 105 m/s (i.e., by a factor of 1.5). Note that the dependence of the maximum velocity on the snowcover thickness is consistent with field measurements. For instance, the avalanche of 10 February 1999 was approximately half as large in terms of deposited volume as the avalanche of 25 February 1999, and its maximum velocity was 25% lower than the maximum velocity recorded on 25 February 1999. This result is of great importance in engineering applications since it means that the maximum velocity and therefore the destructive power of a powder-snow avalanche primarily result from its ability to entrain snow from the snowcover when it descends.

10.6.2 Depth-Averaged Equations

An airborne avalanche is a very turbulent flow of a dilute ice–particle suspension in air. It can be considered as a one-phase flow as a first approximation. Indeed, the Stokes number, defined as the ratio of a characteristic time of the fluid to the relaxation time of the particles, is low, implying that particles adjust quickly to changes in the air motion. At the particle scale, fluid turbulence is high enough to strongly shake the mixture since the particle size is quite small. To take into account particle sedimentation, authors generally consider airborne avalanches as turbulent, stratified flows. Thus, contrary to flowing avalanches, bulk rheological behavior is well identified in the case of airborne avalanches. The main differences between the various models result

from the different boundary conditions, use of the Boussinesq approximation, and the closure equations for turbulence. Parker et al. (1986) developed a complete depth-averaged model for turbidity currents. The equations of motion proposed by these authors are more complicated than the corresponding set for dense flows presented in Section 10.5.2, since they include additional equations arising from the mass balance for the dispersed phase, the mean and turbulent kinetic energy balances, and the boundary conditions related to the entrainment of sediment and surrounding fluid.

$$\frac{\partial h}{\partial t} + \frac{\partial hu}{\partial x} = E_a u, \quad (10.62)$$

$$\frac{\partial(Ch)}{\partial t} + \frac{\partial(hUC)}{\partial x} = v_s E_s - v_s c_b, \quad (10.63)$$

$$\frac{\partial hu}{\partial t} + \frac{\partial hu^2}{\partial x} = RCgh \sin \theta - \frac{1}{2} Rg \frac{\partial Ch^2}{\partial x} - u_*^2, \quad (10.64)$$

$$\begin{aligned} \frac{\partial hK}{\partial t} + \frac{\partial huK}{\partial x} = & \frac{1}{2} E_a u^3 + u_*^2 u - \varepsilon_0 h - \frac{1}{2} E_a u RCgh \\ & - \frac{1}{2} Rgh v_s (2C + E_s - c_b), \end{aligned} \quad (10.65)$$

where u is the mean velocity, h the flow depth, K the mean turbulent kinetic energy, C the mean volume concentration (ratio of particle volume to total volume), E_a a coefficient of entrainment of surrounding fluid into the current, v_s the settlement velocity, E_s a coefficient of entrainment of particles from the bed into the current, c_b the near-bed particle concentration, R the specific submerged gravity of particles (ratio of buoyant density to ambient fluid density), u_*^2 the bed shear velocity, and ε_0 the depth-averaged mean rate of dissipation of turbulent energy due to viscosity. The main physical assumption in Parker *et al.*'s model is that the flow is considered as a one-phase flow in terms of momentum balance, but treated as a two-phase flow concerning the mass balance. Equation (10.62) states that the total volume variation results from entrainment of surrounding fluid. In (10.63), the variation in the mean solid concentration is due to the difference between the rate of particles entrained from the bed and the sedimentation rate. Equation (10.64) is the momentum balance equation. The momentum variation results from the driving action of gravity and the resisting action of bottom shear stress; depending on the flow depth profile, the pressure gradient can contribute to either accelerating or decelerating the flow. Equation (10.65) takes into account the turbulence expenditure for the particles to stay in suspension. Turbulent energy is supplied by the boundary layers (at the flow interfaces with the surrounding fluid and the bottom). Turbulent energy is lost by viscous dissipation ($\varepsilon_0 h$ in (10.65)), mixing the flow (fourth and fifth terms in (10.65)), and maintaining the suspension against sedimentation flow mixing (last term on the right-hand side of (10.65)).

Although originally devoted to submarine turbidity currents, this model has been applied to airborne avalanches with only small modifications in the entrainment functions (Fukushima and Parker, 1990). A new generation of powder-snow avalanche models has recently appeared (Hutter, 1996). Some rely on the numerical resolution of local equations of motion, including a two-phase mixture approximation and closure equations, usually a $k - \epsilon$ model for turbulence (Hutter 1996). A number of researchers believe that a powder-snow avalanche is tightly related to a denser part that supplies the airborne part with snow; these researchers have thus tried to establish the relation existing between a dense core and an airborne avalanche (Eglit 1983; Nazarov 1991; Issler 1998). Though these recent developments are undoubtedly a promising approach to modeling powder-snow avalanches, their level of sophistication contrasts with the crudeness of their basic assumptions as regards the momentum exchanges between phases, turbulence modification due to the dispersed phase, and so on. At this level of our knowledge of physical and natural processes, it is still interesting to continue using simple models and fully exploring what they can describe and explain.

10.7 Comparison with Data

In this chapter, emphasis has been given to presenting the physical features of gravity flows on steep slope and outlining various fluid-mechanics approaches to computing their flow behavior. Since the ultimate goals are to predict how materials are mobilized on a steep slope, how the resulting gravity flow behaves, and how this flow eventually comes to a halt, it is of paramount importance to address the predictive capability of the mathematical models outlined from Section 10.4 to Section 10.6. The question of prediction, a central topic in physical and natural sciences has attracted considerable attention not only from scientists but also from philosophers and sociologists. In the field of geomorphic and geophysical models, contemporary modeling faces special challenges, some of them controversial, such as the relevance of model calibration, the problem of scale between laboratory models and natural events, the uncertainty on the initial and boundary conditions, the random nature versus deterministic behavior of processes, and the making of models (what science philosophers refer to as reductionism and constructionism) and their testing (Wilcock and Iverson 2003).

10.7.1 Comparison with Laboratory Data

In any fluid-mechanics approach, a major impediment to natural flows is the limited availability of relevant data to test models. Ideally, since gravity flows on steep slope involve physical processes that are accessible to direct measurement and observation, we may think of monitoring natural sites and collecting field data to test the models. In some instances (e.g., for snow avalanches), it is even possible to trigger flows, which

opens up the way to quantitative tests that are similar to those of classical physics. Yet, in practice, this road is paved with difficulties of many kinds, some resulting from taking measurements in natural conditions, others stemming from the very nature of the test, for which experimental control is barely possible. Iverson (2003b) best summarized this situation: “The traditional view in geosciences is that the best test of a model is provided by data collected in the field, where processes operate at full complexity, unfettered by artificial constraints. [...] If geomorphology is to make similarly rapid advances, a new paradigm may be required: mechanistic models of geomorphic processes should be tested principally with data collected during controlled, manipulative experiments, not with field data collected under uncontrolled conditions.” In this respect, laboratory experiments have the overwhelming advantage of testing models in a well-controlled environment and for various flow conditions. The disadvantages are related to the scale and similarity issues (Iverson 1997). When working on small scales, it is difficult to guarantee that the experiments are in full similarity with the natural phenomena. (In similitude theory, this implies that all dimensionless numbers that characterize the composition of the materials and the flow dynamics take similar values.) Moreover, in laboratory experiments, natural materials are replaced by simple materials such as glass beads or sand, which may appear as an absurd simplification of natural materials.

As a typical example, we shall focus on the motion of an avalanche of “mud” on a sloping bed. In Section 10.4.2, we have seen that mudflows involve clay-rich materials whose rheological behavior can be considered viscoplastic as a first approximation. To reproduce these flows on the laboratory scale, we first have to find a good candidate that mimics the rheological behavior of clayey materials. For a long time, pure clays such as kaolin and bentonite were used as a substitute for natural clays, but their rheological behavior departs from an ideal viscoplastic fluid described by the Herschel-Bulkley model (10.8), in particular because they exhibit thixotropic behavior. Today polymeric gels such as Carbopol Ultrez 10 are routinely used as Herschel-Bulkley fluids. We conducted experiments with this material in which we released a fixed volume of material (initially at rest in a reservoir) down an inclined flume and tracked the flowing mass using cameras. An ingenious system combining a high-speed camera, and a pattern projector made it possible to reconstruct the free surface of the flow and determine the position of the front as a function of time (Cochard and Ancey 2008). Figure 10.18 shows an example of surface reconstruction in our flume.

Carbopol is a polymer that forms a viscoplastic gel when mixed with water. A volume concentration as low as 0.4% can produce viscoplastic fluids with a yield stress in excess of 100 Pa (i.e., a consistency close to that of cosmetic products like hair gels). To gain insight into the flow dynamics of viscoplastic fluids, we carried out the experiments with different geometries (inclined plane/flume), inclinations (from 0 deg to 24 deg), and initial volumes. Here, we provide only the time variations in the front position for two flume inclinations and two Carbopol concentrations

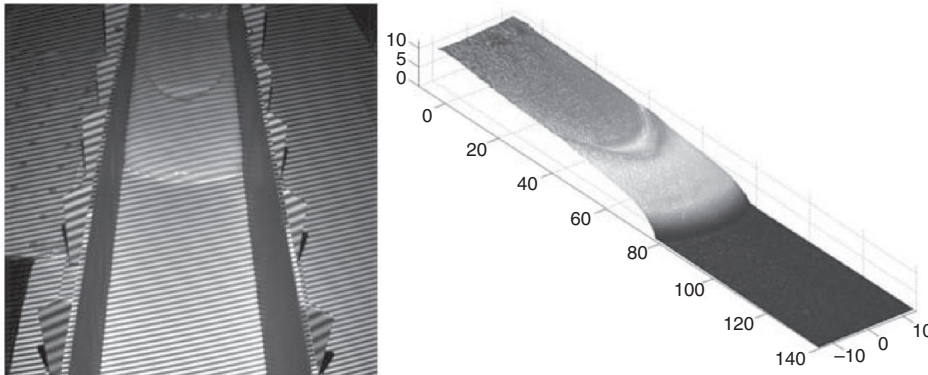


Figure 10.18. Reconstruction of the free surface using image processing. The photograph on the left shows the setup when patterns (here regularly spaced strips) are projected. The picture on the right shows the reconstructed free surface. Data from Cochard and Ancey (2008).

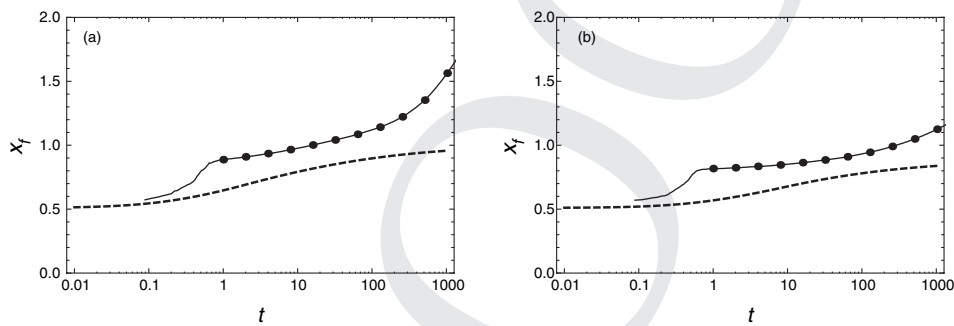


Figure 10.19. Position of the front $x_f(t)$ (in meters) as a function of time t (in seconds) for a flume inclination $\theta = 6$ deg and for two Carbopol concentrations: (a) the concentration is 0.25%; (b) the concentration is 0.3%. The solid line with dots represents the experimental curve, and the dashed line is the analytical solution. Data from Ancey and Cochard (2009).

(0.25 and 0.3%): 6 deg (Figure 10.19) to 24 deg (Figure 10.20); see Ancey and Cochard (2009) and Cochard and Ancey (2009) for additional data. The initial mass was 23 kg. The rheological properties were investigated using a coaxial-cylinder rheometer. A Herschel-Bulkley equation (10.8) was found to properly represent the rheological behavior, and the constitutive parameters were estimated from the rheometrical data. For a Carbopol concentration of 0.25%, $\tau_c = 78$ Pa, $n = 0.39$, and $K = 32.1$ Pa s $^{-n}$, while for a concentration of 0.3%, $\tau_c = 89$ Pa, $n = 0.42$, and $K = 47.7$ Pa s $^{-n}$.

Surprisingly enough, the numerical resolution to the full three-dimensional problem (10.2)–(10.3) is prohibitively complex and requires high-performance computing systems (Rentschler 2010). Time dependence, peculiarities due to rheological properties, along with the existence of a free surface and a contact line, are some of the

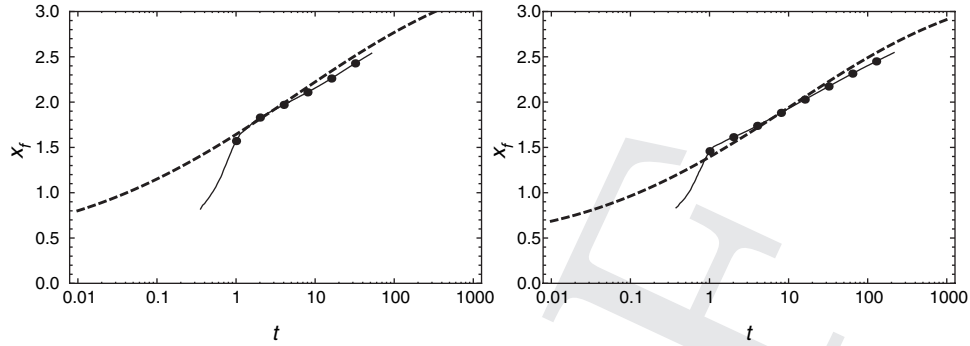


Figure 10.20. Position of the front $x_f(t)$ (in meters) as a function of time t (in seconds) for a flume inclination $\theta = 24$ deg and for two Carbopol concentrations: (a) the concentration is 0.25%; (b) the concentration is 0.3%. The solid line with dots represents the experimental curve, and the dashed line is the analytical solution. Data from Ancy and Cochard (2009).

many complications that arise in the analysis. In spite of this complexity, it is possible to obtain approximate analytical solutions by simplifying the governing equations. In Section 10.5.3, we showed how the assumption of slow and shallow flows made it possible to simplify the governing equations and derive a nonlinear advection diffusion equation for the flow depth (10.45). In this form, this equation is not yet tractable, but using matched asymptotic expansions, we can obtain approximate solutions. For instance, at sufficiently steep slopes, the flow-depth gradient $\partial h/\partial x$ is small compared to the slope $\tan \theta$ in the body region (this approximation no longer holds within the tip region because h drops to zero). As a first approximation (which will form the 0-order term in the asymptotic expansion), we can simplify (10.45) into a nonlinear advection equation:

$$\frac{\partial h}{\partial t} + \tan \theta \frac{\partial}{\partial x} \left[F(h, h_0) \frac{\partial h}{\partial x} \right] = 0, \quad (10.66)$$

with $F = \rho g h_0^2 (3h - h_0) \cos \theta / (6K)$. This equation can be solved analytically, for instance, using the methods of characteristics as shown in Ancy and Cochard (2009). Similar techniques can be used to derive approximations that hold for shallow slopes. In Figures 10.19 and 10.20, we report the theoretical curves together with the experimental data. Recall that the constitutive parameters have been obtained independently; thus, there is no curve adjustment in these plots. Whereas excellent agreement is found at steep slopes (see Figure 10.20), poor agreement is obtained at shallow slopes (see Figure 10.19). Experimental curves systematically exhibited convex shapes at sufficiently long times, whereas the theoretical curves were concave and tended toward an asymptotic value (corresponding to the arrested state). An explanation for this flow acceleration at shallow slope may lie in the formation of lateral levees. At the very beginning, after the material started flowing down the plane, the core of the flow was

strongly sheared, whereas the fluid near the lateral rims was weakly sheared. Once the flow width reached a nearly constant value, the rims “froze” almost instantaneously and formed thick levees. At the same time, a pulse originating from the flow rear overtook the front and gave new impetus to the head. This produced the kink that can be seen in all $x_f(t)$ curves. Indeed, the flow rate remaining nearly constant over some period of time, flow narrowing caused by lateral levees led to swiftly increasing the mean velocity. If this scenario is correct, our two-dimensional analysis is too crude to capture the flow properties, notably the change in the front velocity induced by the levee formation. This explanation, however, remains speculative and calls for more work to elucidate this point.

These experiments illustrate the strengths and weaknesses of many theoretical approaches. Although theory can perform very well for some flow conditions, its predictive capability can be spoiled for other flow conditions unless clear reasons can be found. Many trials are usually needed to evaluate how well a theoretical model performs. Note also that seemingly simple problems such as the motion of a flowing mass of fluid may offer great resistance to analysis and that even today, with high-performance computers, these problems are difficult to solve numerically.

10.7.2 Comparison with Field Data

When testing flow-dynamics models against field data, we face additional challenges. Most of the time, there is no way to measure the constitutive parameters independently (as we did earlier for the Carbopol avalanches), and these must be adjusted from field data, which may bias comparison. Moreover, many input parameters such as the initial volume, the composition of the material, and the volume of entrained/deposited materials are poorly known; some parameters (e.g., the snow density in avalanches) are known to vary a great deal in the course of the flow and setting them to a fixed value (as requested in most models) may make no sense. Finally, taking measurements in natural flows such as avalanches and debris flows, in particular measurements inside the flow, remains a difficult challenge and, as a consequence, we do not have many events fully documented.

Yet, in spite of these numerous impediments, it is possible to obtain relatively accurate descriptions of flow dynamics using simple models as long as one adjusts the model parameters to field data. We illustrate this with two examples. We use field measurements obtained by Gubler et al. (1986) on two snow avalanches in the Aulta and Fogas paths (near Davos, Switzerland). These avalanches exhibited two different behaviors, both of which deserve special mention. We first give the major features of these avalanches, then comment on their flow behavior.

The Aulta avalanche was a large, high-speed, dry-snow avalanche that involved 50,000 m³ of snow. Part of the path is confined within a gully, and the initial flow thickness was in the range 0.7–1 m. The Fogas avalanche was a small, dry-snow

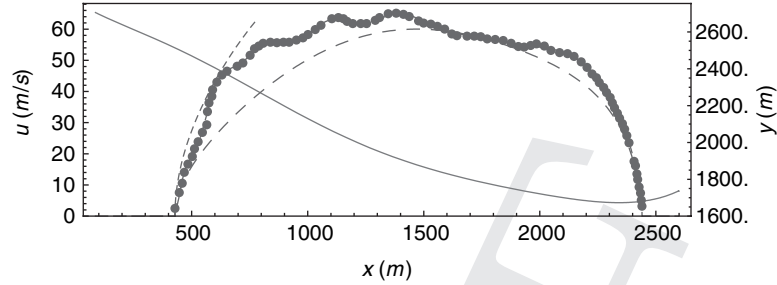


Figure 10.21. Path profile (solid line) of the Aulta site and front velocities (dots) for the 8 February 1984 avalanche. The long dashed curve on the left represents the velocity in a purely inertial regime, computed using equation (10.68), the dashed line illustrates the velocity variation when the Coulomb model is selected (with $\mu = 0.4$ adjusted on the runout distance). Data from Gubler et al. (1986) and Ancey and Meunier (2004).

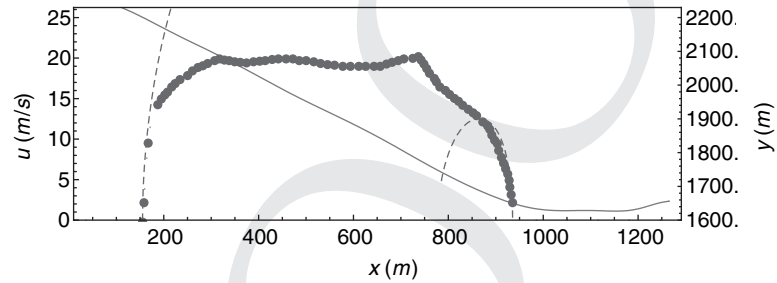


Figure 10.22. Path profile (solid line) of the Fogas site and front velocities (dots) for the 7 March 1985 avalanche. The long dashed curve on the left represents the velocity in a purely inertial regime, computed using equation (10.68), the dashed line on the right illustrates the velocity variation when the Coulomb model is selected (with $\mu = 0.8$ adjusted on the runout distance). Data from Gubler et al. (1986) and Ancey and Meunier (2004).

avalanche that involved 500 m^3 of snow. The path is an unconfined slope, with a fairly regular inclination close to 34° . The initial flow thickness was 30 cm. Gubler et al. (1986) measured the front velocity using a Doppler radar but did not provide the flow-depth variation. Figures 10.21 and 10.22 show the path profiles together with the variation in the front velocity for the Aulta and Fogas avalanches, respectively.

To model these avalanches, we use the flow-depth averaged equations (10.30) with a simplified Coulomb model as constitutive equation: $\tau_b = \mu \rho g h \cos \theta$ and $k = 1$ (Ancey and Meunier 2004; Platzer et al. 2007). We then obtain

$$\frac{\partial \bar{u}}{\partial t} + \bar{u} \frac{\partial \bar{u}}{\partial x} = g \sin \theta - \frac{\tau_b}{\rho h} + g \cos \theta \frac{\partial h}{\partial x}, \quad (10.67)$$

with θ the local path slope, t time, and x the curvilinear abscissa along the path. Note that for curvilinear paths, additional terms should have been added to the equation (Savage and Hutter 1989), but when the topography changes are slow, these terms are

negligible. Just after the release, a large amount of material is suddenly entrained and accelerates vigorously. In the momentum balance equation (10.67), inertia and the pressure gradient must be of the same magnitude, whereas the bottom shear stress has negligible effects. In that case, equation (10.67) is formally identical to the momentum equation of the inviscid shallow-water equations and thus, the dam-break solution (for sloping beds) provides a fairly good approximation of the flow behavior at short times. We expect, most notably, a front-velocity variation in the form

$$u_f \sim gt \sin \theta + u_0 \approx u_0 + \sqrt{2g(x - x_0) \sin \theta}, \quad (10.68)$$

with h_0 the initial flow depth, $u_0 = 2\sqrt{gh_0 \cos \theta}$ the initial velocity (dam-break approximation), x_0 the initial position of the front. This regime is usually referred to as the *inertial phase*. Indeed, it can be shown that once motion of the head begins, the boundary propagates downslope with an acceleration identical to that of a frictionless point mass moving along the slope (Ancy et al. 2008; Mangeney et al. 2010). This finding implies that the boundary speed is uninfluenced by the presence of adjacent fluid after motion commences.

At the end of its course, the flow experiences a *runout phase*, where all its energy is dissipated by friction. The flow behavior is then governed by a balance between the pressure gradient and shear stress (on shallow slopes), which leads to a significant drop in velocity over a fairly short distance. It is straightforward to show that the front velocity u_f decelerates as

$$u_f \sim \sqrt{2g(x_s - x) \cos \theta (\tan \theta - \mu)}, \quad (10.69)$$

where x_s denotes the runout distance (the point of farthest reach).

In Figures 10.21 and 10.22, we have reported the curves corresponding to the inertial and runout phases given by equations (10.68) and (10.69). For the Aulta avalanche, equation (10.68) provides a fairly good approximation of the inertial phase over the first 200 m of the avalanche course. For the Coulomb model, we adjusted the bulk friction coefficient μ for the computed runout distance to match the recorded value. As seen in Figure 10.21, there is relatively good agreement between computed and measured velocities for the runout phase and the agreement is still correct for the earlier flow phases. Note that the flow geometry has been significantly simplified in the computation: In particular, changes in the flow section between the starting area and the flow zone were not taken into account, which may explain why differences between the recorded and measured velocities for x in the range 500–1500 m can be observed. Snow entrainment, which was likely to occur and affect the front velocity, was not considered here. Despite these substantial simplifications, a one-parameter model as simple as the Coulomb model is able to reproduce the front-velocity variations for the Aulta avalanche. The avalanche may have reached a nearly steady regime, but the general trend is an initial acceleration followed by a deceleration after reaching a maximum velocity.

For the Fogas avalanche, the transition from the inertial to nearly steady regimes is quite abrupt and the same holds for the transition between the steady and runout regimes. The inertial and Coulomb approximations hold for a very narrow range of x -values (i.e., in the starting and deposition areas). The important point is that between the inertial and runout phases, equilibrium seems to have been reached over a 400-m length (i.e., half the distance traveled by the avalanche) since velocity was nearly constant and path slope was quite regular.

The relatively good agreement achieved with the Coulomb model is not an isolated occurrence. In a recent survey in which 15 documented avalanches were analyzed (Ancy and Meunier 2004), it was found that for ten events, the Coulomb model was a suitable approximation of the bulk behavior, whereas for five events, there was clearly a velocity dependence on the bulk friction coefficient. For a few events, the bulk frictional force exhibits a dependence on the mean velocity, but no clear trend in the $\tau_b(u)$ dependence was found (Ancy and Meunier 2004). An interesting property of this simple Coulomb block model is that knowing the runout distance (point of furthest reach) of an avalanche makes it possible to infer the μ value. Because avalanche events have been recorded over a long time period at different sites in different alpine regions, we can deduce the statistical properties of the f distribution at different places. If the bulk friction coefficient μ were a true physical parameter, its statistical properties should not vary with space. Ancy thus conducted a statistical analysis on μ values by selecting data from 173 avalanches collected from seven sites in France. These sites are known to produce large avalanches, and their activity has been followed since the beginning of the 20th century. Figure 10.23

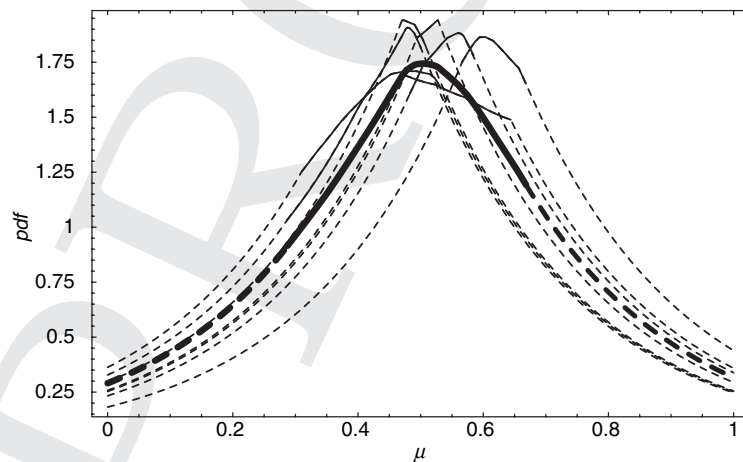


Figure 10.23. Empirical probability distribution functions (pdf) of the 173 μ values collected from seven paths. The thick line represents the distribution function of the total sample, whereas the thin lines are related to individual paths. Each curve has been split into three parts: the central part (solid line) corresponds to the range of computed μ values, and the end parts have been extrapolated. After Ancy (2005).

shows the probability distribution of μ for each site together with the entire sample. Although the curves are close and similar, they are not statistically identical. This means that the probability distribution function of μ is not uniquely determined and depends on other parameters such as snow properties and site configuration. Within this approach, the Coulomb model successfully captures the flow features, but its friction parameter is not a true physical parameter. This, however, should not negate interest of the Coulomb model because, given the number of approximations underpinning the sliding block model, the statistical deviance may originate from crude assumptions.

10.8 Concluding Remarks and Perspectives

Since the pioneering work of Coaz (1881), who initiated the first avalanche survey in the Swiss Alps, and Mougin (1922), who proposed the first avalanche-dynamics model, a huge amount of work has been done to collect field data, develop mathematical models to predict flow behavior, and conduct experiments on various scales (from laboratory to field scales). The subject has become sufficiently mature for conclusions and prospects to be drawn.

The phenomenological knowledge and the modeling of gravity flows such as snow avalanches and debris flows have essentially been motivated by land management issues and engineering applications. Indeed, predicting the runout distance, the impact forces, and the occurrence frequency of rare events are of paramount importance to risk mapping and protection against natural hazards. Even though other tools such as statistical techniques (data correlation, extreme value theory, Bayesian simulation) also have been used to predict extreme events (McClung and Lied 1987; Rickenmann 1999; Meunier and Ancy 2004; Keylock 2005; Eckert et al. 2008), the fluid-mechanics approach has emerged as the most fruitful way of computing the salient characteristics of gravity flows. Since the early 1920s, different generations of models, with increasing levels of sophistication, have been developed. For instance, the earliest dynamic models of avalanche considered snow avalanches as a rigid block (10.23) that experiences a frictional force that accounts for the resistance from the ambient air, the energy dissipation, and possibly momentum transfers (Mougin, 1922; Voellmy, 1955; Bozhinskiy and Losev, 1998). Although the first developments dated back to the 1920s, these very simple models were in use until the 1990s. The second generation of models used the analogy with water floods, which led to governing equations in the form of the flow-depth averaged equations referred to as the Saint-Venant equations (10.28)–(10.29). Although the earliest developments dated back to the 1960s with the work of Salm (1966) and Soviet researchers Grigorian and Eglit (see Bozhinskiy and Losev 1998 for a historical account), it was not until the 1980s that computers and numerical techniques were sufficiently powerful to solve hyperbolic differential equations such as the Saint-Venant equations (Brugnot and Pochat 1981; Vila 1986).

In the early 2000s, the first commercial products based on these equations were made available to engineers (Christen et al., 2002). Models for debris flows followed an evolution similar to that of avalanche-dynamics models, but with a lag time of 10–20 years.

Strikingly, while substantial progress has been achieved over the last 30 years in terms of physical modeling, the gain in accuracy for land management and engineering applications appears much more limited (Salm, 2004). Indeed, a number of problems (e.g., model calibration and values of input parameters) that already existed in the first generation of models have not been fixed and persist, often hidden by the level of complexity of current models, but sometimes exacerbated by the growing differences between variants of the same original model. In the sliding-block models, the frictional parameters could not be measured and were thus fit on field data (Buser and Frutiger 1980; Salm et al. 1990). There is clear evidence that these parameters are more conceptual than physical in that they do not represent a physical process but combine many different physical processes into a single, simple mathematical expression (Meunier et al. 2004). The comparison with field data in Section 10.7.2 provides an example. There is still an avid debate about the rheological law to be used in the depth-averaged equations. A number of models used a Coulomb or a Voellmy empirical law to model bed resistance and internal energy dissipation (Savage and Hutter 1989; Pudasaini and Hutter 2006), which amounts to positing that the rheological behavior can be described using a simple, single-valued expression of the bottom shear stress as a function of the depth-averaged velocity and flow depth. Iverson (2003a) provided evidence that for debris mixtures, the rheological properties cannot be captured using simple constitutive equations (e.g., Newtonian or Herschel-Bulkley laws) since they depend on additional parameters such as the pore pressure or the particle concentration, which may vary significantly within the bulk. The direct consequence is that the depth-averaged equations (10.28)–(10.29) must be supplemented by additional equations that describe the evolution of inner variables such as pore pressure or solids concentration (Iverson and Denlinger 2001; Iverson et al. 2010). Outdoor experiments and field surveys confirmed the substantial time variations in the basal pore pressure in debris flows—variations that reflect changes in the bulk dynamics (McArdell et al. 2006; Iverson et al. 2010). This search of more versatile and robust constitutive equations of natural materials has also entailed the development of models that introduced a large number of parameters. For coarsely parameterized models, some parameters have no physical meaning, and since they cannot be measured independently, their value must be adjusted for the model to match the observations. If this exercise is feasible when the number of parameters is low, it becomes increasingly difficult when this number exceeds three or four parameters. Parsimony and physical meaning of the model parameters are thus two stringent constraints that have made the development of reliable models difficult (Iverson 2003b).

In short, the first generation of models (e.g., the Voellmy model for flowing avalanches, the KS model for powder-snow avalanches) forms a simple but consistent framework that has been extensively used by scientists and engineers. The second generation of models (based on depth-averaged equations) opens many new directions for more realistic predictions, but there are still many points that deserve clarification and further work.

- The constitutive equation of saturated and unsaturated granular mixtures remains a difficult topic. Although there are empirical relations that provide fairly good descriptions of laboratory experiments (Delannay et al. 2007; Forterre and Pouliquen 2008), their generalization and applicability to natural flows are still open questions.
- In most cases, there is mass exchange between the flow and sloping bed. The processes involved in entrainment and deposition have been investigated, in particular through laboratory experiments and numerical simulations (Issler 1998; Princevac et al. 2005; Sovilla and Bartelt 2006; Mangeney et al. 2007, 2010), but many points (e.g., the role of pore pressure fluctuations) are still unclear.
- As highlighted earlier, additional equations that describe the evolution of the material composition are required. Making allowance for particle segregation, variation in the solids concentration, and evolution of the pore pressure are some of the challenges to be addressed.
- There is clear evidence that natural flows can develop complex internal structures (e.g., levees that channelize the flow, bouldery front that may retain the flow behind it, digitate lobate terminations, fingering instabilities, density stratification). (Iverson 1997; Félix and Thomas 2004; Deboeuf et al. 2006; Gray 2010). In the framework of depth-averaged equations, is it possible to account for these inner structures despite the averaging process, or does this mean that a next generation of models is in order?
- Combining stochastic tools and deterministic flow-dynamics models has been attempted to answer a number of questions such as those related to model calibration and the influence of the uncertainties on the input variables and model parameters of stochastic modeling. (Harbitz et al. 2001; Barbolini and Keylock 2002; Meunier and Ancey 2004; Ancey 2005; Dalbey et al. 2008; Gauer et al. 2009). There is crucial need for integrated models, in particular for land use planning and risk mapping, that are able to provide not only the flow features but also the uncertainties on these predictions.

References

- Ancey, C., 2004: Powder-snow avalanches: Approximation as non-Boussinesq clouds with a Richardson-number-dependent entrainment function. *J. Geophys. Res.* **109**, F01005.
- Ancey, C., 2005: Monte Carlo calibration of avalanches described as Coulomb fluid flows. *Phil. Trans. Roy. Soc. London A* **363**, 1529–1550.
- Ancey, C., 2007: Plasticity and geophysical flows: A review. *J. Non-Newtonian Fluid Mech.* **142**, 4–35.
- Ancey, C., and S. Cochard, 2009: The dam-break problem for Herschel-Bulkley fluids down steep flumes. *J. Non-Newtonian Fluid Mech.* **158**, 18–35.
- Ancey, C., S. Cochard, and N. Andreini, 2009: The dam-break problem for viscous fluids in the high-capillary-number limit. *J. Fluid Mech.* **624**, 1–22.

- Ancey, C., S. Cochard, S. Wiederseiner, and M. Rentschler, 2006: Front dynamics of supercritical non-Boussinesq gravity currents. *Water Resour. Res.* **42**, W08424.
- Ancey, C., S. Cochard, S. Wiederseiner, and M. Rentschler, 2007: Existence and features of similarity solutions for supercritical non-Boussinesq gravity currents. *Physica D* **226**, 32–54.
- Ancey, C., and P. Evesque, 2000: Frictional-collisional regime for granular suspension flows down an inclined channel. *Phys. Rev. E* **62**, 8349–8360.
- Ancey, C., C. Gervasoni, and M. Meunier, 2004: Computing extreme avalanches. *Cold Reg. Sci. Technol.* **39**, 161–180.
- Ancey, C., R. M. Iverson, M. Rentschler, and R. P. Denlinger, 2008: An exact solution for ideal dam-break floods on steep slopes. *Water Resour. Res.* **44**, W01430.
- Ancey, C., and M. Meunier, 2004: Estimating bulk rheological properties of flowing snow avalanches from field data. *J. Geophys. Res.* **109**, F01004.
- Balmforth, N. J., and R. V. Craster, 1999: A consistent thin-layer theory for Bingham plastics. *J. Non-Newtonian Fluid Mech.* **84**, 65–81.
- Balmforth, N. J., R. V. Craster, and R. Sassi, 2002: Shallow viscoplastic flow on an inclined plane. *J. Fluid Mech.* **470**, 1–29.
- Balmforth, N. J., and R. R. Kerswell, 2005: Granular collapse in two dimensions. *J. Fluid Mech.* **538**, 399–428.
- Barbolini, M., and C. J. Keylock, 2002: A new method for avalanche hazard mapping using a combination of statistical and deterministic models. *Nat. Hazard Earth. Sys. Sci.* **2**, 239–245.
- Bartelt, P., and B. W. McArdell, 2009: Granulometric investigations of snow avalanches. *J. Glac.* **55**, 829–833.
- Beghin, P., and G. Brugnot, 1983: Contribution of theoretical and experimental results to powder-snow avalanche dynamics. *Cold Regions Sci. Technol.* **8**, 63–73.
- Beghin, P., E. J. Hopfinger, and R. E. Britter, 1981: Gravitational convection from instantaneous sources on inclined boundaries. *J. Fluid Mech.* **107**, 407–422.
- Beghin, P., and X. Olagne, 1991: Experimental and theoretical study of the dynamics of powder snow avalanches. *Cold Reg. Sci. Technol.* **19**, 317–326.
- Benjamin, T. B., 1968: Gravity currents and related phenomena. *J. Fluid Mech.* **31**, 209–248.
- Bouchut, F., A. Mangeney-Castelnau, B., Perthame, and J.-P. Vilotte, 2003: A new model of Saint Venant and Savage-Hutter type for gravity driven shallow flows. *C. R. Acad. Sci. Paris Sér. I* **336**, 531–536.
- Bozhinskiy, N., and K. S. Losev, 1998: The fundamentals of avalanche science. *Tech. Rep.* 55. EISFL.
- Brugnot, G., and R. Pochat, 1981: Numerical simulation study of avalanches. *J. Glaciol.* **27**, 77–88.
- Bursik, M., A. Patra, E. B. Pitman, C. C. Nichita, J. L. Macias, R. Saucedo, and O. Girina, 2005: Advances in studies of dense volcanic granular flows. *Rep. Prog. Phys.* **68**, 271–301.
- Buser, O., and H. Frutiger, 1980: Observed maximum runout distance of snow avalanches and determination of the friction coefficients μ and ξ . *J. Glaciol.* **26**, 121–130.
- Chambon, G., A. Ghemmour, and D. Laigle, 2009: Gravity-driven surges of a viscoplastic fluid: an experimental study. *J. Non-Newtonian Fluid Mech.* **158**, 54–62.
- Chang, C., and R. L. Powell, 1994: Effect of particle size distributions on the rheology of concentrated bimodal suspensions. *J. Rheol.* **38**, 85–98.
- Chow, V. T. (ed.), 1959: *Open-Channel Hydraulics*. Mc Graw Hill, New York.
- Christen, M., P. Bartelt, U. and Gruber, 2002: *AVALID: Numerische Berechnung von Fließ- und Staublawinen*. Eidgenössisches Institut für Schnee- und Lawinenforschung, Davos.

- Chugunov, V., J. M. N. T. Gray, and K. Hutter, 2003: Group theoretic methods and similarity solutions of the Savage-Hutter equations. In: K. Hutter and N. Kirchner (eds.), *Dynamics Response of Granular and Porous Materials under Large and Catastrophic Deformations*, pp. 251–261. Springer, Berlin.
- Clague, J. J., and S. G. Evans, 2000: A review of catastrophic drainage of moraine-dammed lakes in British Columbia. *Quaternary Sci. Rev.* **19**, 1763–1783.
- Coaz, J. W., 1881: *Die Lawinen der Schweizer Alpen*. Schmid-Franke, Bern.
- Cochard, S., and C. Ancey, 2008: Tracking the free surface of time-dependent flows: Image processing for the dam-break problem. *Exper. Fluids* **44**, 59–71.
- Cochard, S., and C. Ancey, 2009: Experimental investigation into the spreading of viscoplastic fluids on inclined planes. *J. Non-Newtonian Fluid Mech.* **158**, 73–84.
- Contreras, S. M., and T. R. H. Davies, 2000: Coarse-grained debris-flows: Hysteresis and time-dependent rheology. *J. Hydraul. Eng.* **126**, 938–941.
- Coussot, P., 1997: *Mudflow Rheology and Dynamics*. Balkema, Rotterdam.
- Coussot, P., S. Proust, and C. Ancey, 1996: Rheological interpretation of deposits of yield stress fluids. *J. Non-Newtonian Fluid Mech.* **66**, 55–70.
- Cui, X., J. M. N. T. Gray, and T. Jóhannesson, 2007: Deflecting dams and the formation of oblique shocks in snow avalanches at Flateyri, Iceland. *J. Geophys. Res.* **122**, F04012.
- Dalbey, K., A. Patra, E. B. Pitman, M. I. Bursik, and M. Sheridan, 2008: Input uncertainty propagation methods and hazard mapping of geophysical mass flows. *J. Geophys. Res.* **113**, B05203.
- Davies, T. R. H., 1986: Large debris flow: a macro-viscous phenomenon. *Acta Mech.* **63**, 161–178.
- Deboeuf, S., E. Lajeunesse, O. Dauchot, and B. Andreotti, 2006: Flow rule, self-channelization, and levees in unconfined granular flows. *Phys. Rev. Lett.* **97**, 158303.
- Delannay, R., M. Louge, P. Richard, N. Taberlet, and A. Valance, 2007: Towards a theoretical picture of dense granular flows down inclines. *Nature Mater.* **6**, 99–108.
- Dent, J. D., and T. E. Lang, 1980: Modelling of snow flow. *J. Glaciol.* **26**, 131–140.
- Dent, J. D., and T. E. Lang, 1982: Experiments on the mechanics of flowing snow. *Cold Reg. Sci. Technol.* **5**, 243–248.
- Eckert, N., E. Parent, M. Naaim, and D. Richard, 2008: Bayesian stochastic modelling for avalanche predetermination: From a general system framework to return period computations. *Stoch. Env. Res. Risk Ass.* **22**, 185–206.
- Eglit, E. M., 1983: Some mathematical models of snow avalanches. In: M. Shahinpoor (ed.) *Advances in the Mechanics and the Flow of Granular Materials*, pp. 577–588. Trans Tech Publications, Clausthal-Zellerfeld.
- Ellison, T. H., and J. S. Turner, 1959: Turbulent entrainment in stratified flows. *J. Fluid Mech.* **6**, 423–448.
- Elverhøi, A., D. Issler, F. V. De Blasio, T. Ilstad, C. B. Harbitz, and P. Gauer, 2005: Emerging insights into the dynamics of submarine debris flows. *Nat. Hazard Earth. Sys. Sci.* **5**, 633–648.
- Fannin, R. J., and T. P. Rollerson, 1993: Debris flows: Some physical characteristics and behaviour. *Can. Geotech. J.* **30**, 71–81.
- Félix, G., and N. Thomas, 2004: Relation between dry granular flow regimes and morphology of deposits: Formation of levées in pyroclastic deposits. *Earth Planet. Sci. Lett.* **221**, 197–213.
- Fernández-Nieto, E. D., P. Noble, and J.-P. Vila, 2010: Shallow water equation for non-Newtonian fluids. *J. Non-Newtonian Fluid Mech.* **165**, 712–732.
- Fernando, H. J. S., 1991: Turbulent mixing in stratified fluids. *Annu. Rev. Fluid Mech.* **23**, 455–493.

- Forterre, Y., and O. Pouliquen, 2008: Flows of dense granular media. *Annu. Rev. Fluid Mech.* **40**, 1–24.
- Fukushima, Y., T. Hagihara, and M. Sakamoto, 2000: Dynamics of inclined suspension thermals. *Fluid Dyn. Res.* **26**, 337–354.
- Fukushima, Y., and G. Parker, 1990: Numerical simulation of powder-snow avalanches. *J. Glaciol.* **36**, 229–237.
- Gauer, P., and D. Issler, 2003: Possible erosion mechanisms in snow avalanches. *Ann. Glaciol.* **38**, 384–392.
- Gauer, P., Z. Medina-Cetina, K. Lied, and K. Kristensen, 2009: Optimization and probabilistic calibration of avalanche-block models. *Cold Reg. Sci. Technol.* **59**, 251–258.
- Gratton, J., and C. Vigo, 1994: Self-similar gravity currents with variable inflow revisited: plane currents. *J. Fluid Mech.* **258**, 77–104.
- Gray, J. M. N. T., 2010: Particle size segregation in granular avalanches: A brief review of recent progress. In: J. D. Goddard, J. T. Jenkins and P. Giovine (eds.), *IUTAM-ISIMM Symposium on Mathematical Modeling and Physical Instances of Granular Flows*, vol. 1227, pp. 343–362. AIP, Melville, NY.
- Gray, J. M. N. T., and C. Ancey, 2009: Particle size-segregation, recirculation, and deposition at coarse particle rich flow fronts. *J. Fluid Mech.* **629**, 387–423.
- Gray, J. M. N. T., and B. P. Kokelaar, 2010: Large particle segregation, transport and accumulation in granular free-surface flows. *J. Fluid Mech.* **652**, 105–137.
- Gray, J. M. N. T., M. Wieland, and K. Hutter, 1998: Gravity-driven free surface flow of granular avalanches over complex basal topography. *Proc. R. Soc. London Ser. A* **455**, 1841–1874.
- Gubler, H., M. Hiller, G. Klausegger, and U. Suter, 1986: Messungen an Fließlawinen. *Tech. Rep.* 41. SLF.
- Hallworth, M. A., A. Hogg, and H. E. Huppert, 1998b: Effects of external flow on compositional and particle gravity currents. *J. Fluid Mech.* **359**, 109–142.
- Hampton, M. A., H. J. Lee, and J. Locat, 1996: Submarine landslides. *Rev. Geophys.* **34**, 33–59.
- Harbitz, C., A. Harbitz, and F. Nadim, 2001: On probability analysis in snow avalanche hazard zoning. *Ann. Glaciol.* **32**, 290–298.
- Hogg, A. J., 2006: Lock-release gravity currents and dam-break flows. *J. Fluid Mech.* **569**, 61–87.
- Hogg, A. J., and G. P. Matson, 2009: Slumps of viscoplastic fluids on slopes. *J. Non-Newtonian Fluid Mech.* **158**, 101–112.
- Hogg, A. J., and D. Pritchard, 2004: The effects of hydraulic resistance on dam-break and other shallow inertial flows. *J. Fluid Mech.* **501**, 179–212.
- Hogg, A. J., M. Ungarish, and H. E. Huppert, 2000: Particle-driven gravity currents: asymptotic and box model solutions. *Eur. J. Mech. B. Fluids* **19**, 139–165.
- Hogg, A. H., and A. W. Woods, 2001: The transition from inertia- to bottom-drag-dominated motion of turbulent gravity current. *J. Fluid Mech.* **449**, 201–224.
- Holmes, M. H., 1995: *Introduction to Perturbation Methods*. Springer Verlag, New York.
- Hopfinger, E. J., and J.-C. Tochon-Danguy, 1977: A model study of powder-snow avalanches. *J. Glaciol.* **81**, 343–356.
- Huang, X., and M. H. García, 1997: A perturbation solution for Bingham-plastic mudflows. *J. Hydraul. Eng.* **123**, 986–994.
- Huang, X., and M. H. García, 1998: A Herschel-Bulkley model for mud flow down a slope. *J. Fluid Mech.* **374**, 305–333.
- Hunt, B., 1994: Newtonian fluid mechanics treatment of debris flows and avalanches. *J. Hydraul. Eng.* **120**, 1350–1363.

- Huppert, H. E., W. B., and Dade, 1998: Natural disasters: explosive volcanic eruptions and gigantic landslides. *Theor. Comput. Fluid Dyn.* **10**, 202–212.
- Hürlimann, M., D. Rickenmann, and C. Graf, 2003: Field and monitoring data of debris-flow events in the Swiss Alps. *Can. Geotech. J.* **40**, 161–175.
- Hutter, K., 1996: Avalanche dynamics. In: V. P. Singh (ed.), *Hydrology of Disasters*, pp. 317–392. Kluwer Academic Publications, Dordrecht.
- Issler, D., 1998: Modelling of snow entrainment and deposition in powder-snow avalanches. *Ann. Glaciol.* **26**, 253–258.
- Issler, D., 2003: Experimental information on the dynamics of dry-snow avalanches. In: K. Hutter and N. Kirchner (eds.), *Dynamic Response of Granular and Porous Materials Under Large and catastrophic Deformation* pp. 109–160. Springer, Berlin.
- Iverson, R. M., 1997: The physics of debris flows. *Rev. Geophys.* **35**, 245–296.
- Iverson, R. M., 2003a: The debris-flow rheology myth. In: C. L. Chen and D. Rickenmann (eds.), *Debris Flow Mechanics and Mitigation Conference*, pp. 303–314. Davos: Mills Press.
- Iverson, R. M., 2003b: How should mathematical models of geomorphic processes be judged? In: P. R. Wilcock and R. M. Iverson (ed.), *Prediction in Geomorphology*, pp. 83–94. American Geophysical Union, Washington, DC.
- Iverson, R. M., 2005: Debris-flow mechanics. In: M. Jakob and O. Hungr (eds.), *Debris-Flow Hazards and Related Phenomena*, pp. 105–134. Springer, Berlin.
- Iverson, R. M., and R. P. Denlinger, 2001: Flow of variably fluidized granular masses across three-dimensional terrain. I. Coulomb mixture theory. *J. Geophys. Res.* **106**, 537–552.
- Iverson, R. M., M. Logan, and R. G. LaHusen, 2010: The perfect debris flow? Aggregated results from 28 large-scale experiments. *J. Geophys. Res.* **115**, F03005.
- Iverson, R. M., M. E. Reid, and R. G. LaHusen, 1997: Debris-flow mobilization from landslides. *Annu. Rev. Earth. Planet. Sci.* **25**, 85–138.
- Iverson, R. M., and J. Vallance, 2001: New views of granular mass flows. *Geology* **29**, 115–118.
- Johnson, A. M., and J. R. Rodine, 1984: Debris flow. In: D. Brunsten and D. B. Prior (eds.), *Slope Instability*, pp. 257–362. John Wiley and Sons, Chichester.
- Jomelli, V., and P. Bertran, 2001: Wet snow avalanche deposits in the French Alps: Structure and sedimentology. *Geografiska Annaler Series A—Physical Geography* **83**, 15–28.
- Jop, P., Y. Forterre, and O. Pouliquen, 2005: Crucial role of side walls for granular surface flows: Consequences for the rheology. *J. Fluid Mech.* **541**, 167–192.
- Josserand, C., P.-Y. Lagrée, and D. Lhuillier, 2004: Stationary shear flows of dense granular materials: A tentative continuum modelling. *Eur. Phys. J. E* **14**, 127–135.
- Karelsky, K. V., V. V. Papkov, A. S. Petrosyan, and D. V. Tsygankov, 2000: Particular solutions of shallow-water equations over a non-flat surface. *Phys. Lett. A* **271**, 341–348.
- Keller, J. B., 2003: Shallow-water theory for arbitrary slopes of the bottom. *J. Fluid Mech.* **489**, 345–348.
- Kern, M. A., P. Bartelt, B. Sovilla, and O. Buser, 2009: Measured shear rates in large dry and wet snow avalanches. *J. Glaciol.* **55**, 327–338.
- Kern, M. A., F. Tiefenbacher, and J. N. McElwaine, 2004: The rheology of snow in large chute flows. *Cold Reg. Sci. Technol.* **39**, 181–192.
- Kerswell, R. R., 2005: Dam break with Coulomb friction: a model for granular slumping? *Phys. Fluids* **17**, 057101.
- Keylock, C. J., 2005: An alternative form for the statistical distribution of extreme avalanche runout distances. *Cold Reg. Sci. Technol.* **42**, 185–193.
- Kulikovskiy, A. G., and E. I. Svechnikova, 1977: Model dlja rascheta dvizhija pilevoi snezhnoi lavini (a model for computing powdered snow avalanche motion) [in Russian]. *Materiali Glatsiologicheskikh Issledovanii [Data of Glaciological Studies]* **31**, 74–80.

- Legros, F., 2002: The mobility of long-runout landslides. *Eng. Geol.* **63**, 301–331.
- Leighton, D., and A. Acrivos, 1987: The shear-induced migration of particles in a concentrated suspensions. *J. Fluid Mech.* **181**, 415–439.
- LeVeque, R. J., 2002: *Finite Volume Methods for Hyperbolic Problems*. Cambridge University Press, Cambridge.
- Lighthill, M. J., and G. B. Whitham, 1955: On kinematic waves. I. Flood movement in long rivers. *Proc. R. Soc. London Ser. A* **229**, 281–316.
- Linares-Guerrero, E., C. Goujon, and R. Zenit, 2007: Increased mobility of bidisperse granular avalanches. *J. Fluid Mech.* **593**, 475–504.
- Liu, K. F. and C. C. Mei, 1990a: Approximate equations for the slow spreading of a thin sheet of Bingham plastic fluid. *Phys. Fluids A* **2**, 30–36.
- Liu, K. F., and C. C. Mei, 1990b: Slow spreading of a sheet of Bingham fluid on an inclined plane. *J. Fluid Mech.* **207**, 505–529.
- Lootens, D., H. Van Damme, and P. Hébraud, 2003: Giant stress fluctuations at the jamming transition. *Phys. Rev. Lett.* **90**, 178301.
- Maeno, O., 1993: Rheological characteristics of snow flows. In: *International Workshop on Gravitational Mass Movements* (ed. L. Buisson and G. Brugnot), pp. 209–220. Cemagref, Grenoble.
- Major, J. J., and T. C. Pierson, 1992: Debris flow rheology: Experimental analysis of fine-grained slurries. *Water Resour. Res.* **28**, 841–857.
- Mangeny, A., P. Heinrich, and R. Roche, 2000: Analytical solution for testing debris avalanche numerical models. *Pure Appl. Geophys.* **157**, 1081–1096.
- Mangeny, A., O. Roche, O. Hungr, N. Mangold, G. Faccanoni, and A. Lucas, 2010: Erosion and mobility in granular collapse over sloping beds. *J. Geophys. Res.* **115**, F03040.
- Mangeny, A., L. S., Tsimring, I. S., Volfson, and F. Bouchut, 2007: Avalanche mobility induced by the presence of an erodible bed and associated entrainment. *Geophys. Res. Lett.* **34**, L22401.
- Marquez, M., A. Robben, B. P. Grady, and I. Robb, 2006: Viscosity and yield stress reduction in non-colloidal concentrated suspensions by surface modification with polymers and surfactants and/or nanoparticle addition. *J. Colloid. Interface Sci.* **295**, 374–387.
- Matson, G. P., and A. J. Hogg, 2007: Two-dimensional dam break flows of Herschel-Bulkley fluids: The approach to the arrested state. *J. Non-Newtonian Fluid Mech.* **142**, 79–94.
- McArdell, B. W., P. Bartelt, and J. Kowalski, 2006: Field observations of basal forces and fluid pore pressure in a debris flow. *Geophys. Res. Lett.* **34**, L07406.
- McClung, D. M., and K. Lied, 1987: Statistical and geometrical definition of snow avalanche runout. *Cold Reg. Sci. Technol.* **13**, 107–119.
- McElwaine, J. N., 2005: Rotational flow in gravity current heads. *Phil. Trans. Roy. Soc. London A* **363**, 1603–1623.
- Mei, C. C., K. F. Liu, and M. Yuhi, 2001: Mud flows—Slow and fast. In: N. J. Balmforth and A. Provenzale (eds.), *Geomorphological Fluid Mechanics: Selected topics in geological and geomorphological fluid mechanics*, pp. 548–577. Springer, Berlin.
- Mei, C. C., and M. Yuhi, 2001: Slow flow of a Bingham fluid in a shallow channel of finite width. *J. Fluid Mech.* **431**, 135–159.
- Meunier, M., and C. Ancey, 2004: Towards a conceptual approach to predetermining long-return-period avalanche run-out distances. *J. Glaciol.* **50**, 268–278.
- Meunier, M., C. Ancey, and J.-M. Taillandier, 2004: Fitting avalanche-dynamics models with documented events from the Col du Lautaret site (France) using the conceptual approach. *Cold Regions Sci. Technol.* **39**, 55–66.
- Morris, J. F., 2009: A review of microstructure in concentrated suspensions and its implications for rheology and bulk flow. *Rheol. Acta* **48**, 909–923.

- Morris, J. F., and F. Boulay, 1999: Curvilinear flows of noncolloidal suspensions: The role of normal stresses. *J. Rheol.* **43**, 1213–1238.
- Mougin, P., 1922: *Les avalanches en Savoie*, vol. IV. Ministère de l'Agriculture, Direction Générale des Eaux et Forêts, Service des Grandes Forces Hydrauliques, Paris.
- Nazarov, A. N., 1991: Mathematical modelling of a snow-powder avalanche in the framework of the equations of two-layer shallow water. *Fluid Dyn.* **12**, 70–75.
- Norem, H. F., F. Irgens, and B. Schieldrop, 1986: A continuum model for calculating snow avalanche velocities. In: H. Gubler and B. Salm (eds.), *Avalanche Formation, Movement and Effects*, pp. 363–379. IAHS, Wallingford, Oxfordshire, UK, Davos.
- Osmond, D. I., and R. W. Griffiths, 2001: The static shape of yield strength fluids slowly emplaced on slopes. *J. Geophys. Res.* **B 106**, 16241–16250.
- Ottino, J. M., and D. V. Khakhar, 2000: Mixing and segregation of granular materials. *Annu. Rev. Fluid Mech.* **32**, 55–91.
- Ovarlez, G., F. Bertrand, and S. Rodts, 2006: Local determination of the constitutive law of a dense suspension of noncolloidal particles through magnetic resonance imaging. *J. Rheol.* **50**, 259–292.
- Parker, G., 1982: Conditions for the ignition of catastrophically erosive turbidity currents. *Mar. Geol.* **46**, 307–327.
- Parker, G., Y. Fukushima, and H. M. Pantin, 1986: Self-accelerating turbidity currents. *J. Fluid Mech.* **171**, 145–181.
- Parsons, J. D., K. X. Whipple, and A. Simoni, 2001: Experimental study of the grain-flow, fluid-mud transition in debris flows. *J. Geol.* **109**, 427–447.
- Phillips, J. C., A. J. Hogg, R. R. Kerswell, and N. Thomas, 2006: Enhanced mobility of granular mixtures of fine and coarse particles. *Earth Planet. Sci. Lett.* **246**, 466–480.
- Piau, J.-M., 1996: Flow of a yield stress fluid in a long domain. Application to flow on an inclined plane. *J. Rheol.* **40**, 711–723.
- Platzer, K., P. Bartelt, and M. A. Kern, 2007: Measurements of dense snow avalanche basal shear to normal stress ratios (S/N). *Geophys. Res. Lett.* **34**, L07501.
- Pouliquen, O., and Y. Forterre, 2002: Friction law for dense granular flow: Application to the motion of a mass down a rough inclined plane. *J. Fluid Mech.* **453**, 133–151.
- Princevac, M., H. J. S. Fernando, and C. D. Whiteman, 2005: Turbulent entrainment into natural gravity-driven flows. *J. Fluid Mech.* **533**, 259–268.
- Pudasaini, S. P., and K. Hutter, 2003: Rapid shear flows of dry granular masses down curved and twisted channels. *J. Fluid Mech.* **495**, 193–208.
- Pudasaini, S. P., and K. Hutter, 2006: *Avalanche Dynamics*. Berlin, Springer.
- de Quervain, R., 1981: *Avalanche Atlas*. Unesco, Paris.
- Rammer, L., M. A. Kern, U. Gruber, and F. Tiefenbacher, 2007: Comparison of avalanche-velocity measurements by means of pulsed Doppler radar, continuous wave radar and optical methods. *Cold Reg. Sci. Technol.* **54**, 35–54.
- Rentschler, M., 2010: Simulating viscoplastic avalanches. PhD thesis, École Polytechnique Fédérale de Lausanne.
- Rickenmann, D., 1999: Empirical relationships for debris flows. *Nat. Hazard* **19**, 47–77.
- Salm, B., 1966: Contribution to avalanche dynamics. In: *Scientific Aspects of Snow and Ice Avalanche*, pp. 199–214. IAHS Press, Wallingford, Oxfordshire, UK, Davos.
- Salm, B., 2004: A short and personal history of snow avalanche dynamics. *Cold Reg. Sci. Technol.* **39**, 83–92.
- Salm, B., A. Burkard, and H. Gubler, 1990: Berechnung von Fliesslawinen, eine Anleitung für Praktiker mit Beispielen. *Tech. Rep.* No 47. Eidgenössisches Institut für Schnee- und Lawinenforschung (Davos).
- Savage, S. B., 1982: Granular flows down rough inclined—Review and extension. In: J. T. Jenkins and M. Satake (eds.), *U.S./Japan Seminar on New Models and*

- Constitutive Relations in the Mechanics of Granular Materials*, pp. 261–282. Elsevier Science Publishers, Amsterdam, Ithaca.
- Savage, S. B., 1989: Flow of granular materials. In: P. Germain, J.-M. Piau, and D. Caillerie (eds.), *Theoretical and Applied Mechanics*, pp. 241–266. Elsevier, Amsterdam.
- Savage, S. B., and K. Hutter, 1989: The motion of a finite mass of granular material down a rough incline. *J. Fluid Mech.* **199**, 177–215.
- Savage, S. B., and K. Hutter, 1991: The dynamics of avalanches of granular materials from initiation to runout. Part I: Analysis. *Acta Mech.* **86**, 201–223.
- Savage, S. B., and Y. Nohguchi, 1988: Similarity solutions for avalanches of granular materials down curved bed. *Acta Mech.* **75**, 153–174.
- Sengun, M. Z., and R. F. Probst, 1989: Bimodal model of slurry viscosity with applications to coal slurries. Part 1. Theory and experiment. *Rheol. Acta* **28**, 382–393.
- Siavoshi, S., and A. Kudrolli, 2005: Failure of a granular step. *Phys. Rev. E* **71**, 051302.
- Simpson, J. E., 1972: Effects of a lower boundary on the head of a gravity current. *J. Fluid Mech.* **53**, 759–768.
- Simpson, J. E., 1997: *Gravity Currents in the Environment and the Laboratory*. Cambridge University Press, Cambridge.
- Singh, A., A. Nir, and R. Semiat, 2006: Free-surface flow of concentrated suspensions. *Int. J. Multiphase Flow* **32**, 775–790.
- Siviglia, A., and A. Cantelli, 2005: Effect of bottom curvature on mudflow dynamics: Theory and experiments. *Water Resour. Res.* **41**, W11423.
- Sovilla, B., and P. Bartelt, 2006: Field experiments and numerical modeling of mass entrainment in snow avalanches. *J. Geophys. Res.* **111**, F03007.
- Stickel, J. J., and R. L. Powell, 2005: Fluid mechanics and rheology of dense suspensions. *Annu. Rev. Fluid Mech.* **37**, 129–149.
- Tai, Y.-C., K. Hutter, and J. M. N. T. Gray, 2001: Dense granular avalanches: mathematical description and experimental validation. In: N. J. Balmforth and A. Provenzale (eds.), *Geomorphological Fluid Mechanics*, pp. 339–366. Springer, Berlin.
- Timberlake, B. D., and J. F. Morrison, 2005: Particle migration and free-surface topography in inclined plane flow of a suspension. *J. Fluid Mech.* **538**, 309–341.
- Tognacca, C., 1997: Debris-flow initiation by channel-bed failure. In: C. L. Chen (ed.), *First International Conference on Debris Flow Hazards Mitigation*, pp. 44–53. ASCE, New-York.
- Tsai, J.-C., W. Losert, and G. A. Voth, 2001: Two-dimensional granular Poiseuille flow on an incline: Multiple dynamical regimes. *Phys. Rev. E* **65**, 011306.
- Turnbull, B., J. McElwaine, and C. Ancey, 2007: The Kulikovskiy–Sveshnikova–Beghin model of powder snow avalanches: Development and application. *J. Geophys. Res.* **112**, F01004.
- Turner, J. S., 1973: *Buoyancy Effects in Fluids*. Cambridge University Press, Cambridge.
- Ungarisch, M., 2009: *An Introduction to Gravity Currents and Intrusions*. CRC Publishers, Boca Raton.
- VanDine, D. F., 1985: Debris flows and debris torrents in the Southern Canadian Cordillera. *Can. Geotech. J.* **22**, 44–68.
- Vila, J. P., 1986: Sur la théorie et l’approximation numérique des problèmes hyperboliques non-linéaires, application aux équations de Saint-Venant et à la modélisation des avalanches denses. Ph. D. thesis, Paris VI.
- Voellmy, A., 1955: Über die Zerstörungskraft von Lawinen. *Schweizerische Bauzeitung* **73**, 159–162, 212–217, 246–249, 280–285.
- Voight, B., 1990: The 1985 Nevado del Ruiz volcano catastrophe: Anatomy and retrojection. *J. Volcan. Geoth. Res.* **44**, 349–386.

- Wilcock, P. R., and R. M. Iverson, eds., 2003: *Prediction in Geomorphology*. American Geophysical Union, Washington, DC.
- Zanuttigh, B., and A. Lamberti, 2007: Instability and surge development in debris flows. *Rev. Geophys.* **45**, RG3006.
- Zarraga, I. E., D. A. Hill, and D. T. Leighton, 2000: The characterization of the total stress of concentrated suspensions of noncolloidal spheres in Newtonian fluids. *J. Rheol.* **44**, 185–221.
- Zimmermann, M., P. Mani, P. Gamma, P. Gsteiger, O. Heiniger, and G. Hunziker, 1997: *Murganggefahr und Klimaänderung – ein GIS-basierter Ansatz*. VDF, Zürich.

PROOF